Summer 2016

Radiation noise source modeling and near-field coupling estimation in RF interference

Liang Li

RADIATION NOISE SOURCE MODELING AND NEAR-FIELD COUPLING

ESTIMATION IN RF INTERFERENCE

by

LIANG LI

A THESIS

Presented to the Faculty of the Graduate School of the

MISSOURI UNIVERSITY OF SCIENCE AND TECHNOLOGY

In Partial Fulfillment of the Requirements for the Degree

MASTER OF SCIENCE IN ELECTRICAL ENGINEERING

2016

Approved by

Dr. Jun Fan, Advisor
Dr. Daryl Beetner
Dr. David Pommerenke

ABSTRACT

With increasing complexities and shrinking size of modern electronic devices, the near-field RF interference issues are becoming challenging for RF-digital mixed circuit design. Predicting the coupling from digital module to RF antennas and mitigating RF interference is important to the system performance. The ultimate goal of this study is to address the desensitization issues existing in modern electronic devices that have mixed high speed digital-RF circuits, such as cellphone and wearable devices.

In order to estimate the near-field noise coupling from digital module to RF antennas, the noise source is anticipated to be replaced by its equivalent radiation model which can facilitate the near-field coupling analysis. This thesis focuses on modeling of radiation noise source and its application in RF interference applications. Two methods are proposed, equivalent dipole moment model and Huygens's equivalent model. The methodology of both methods will be introduced and later validated with full-wave simulation and measurement. Dipole moment model is extracted by Least-square and improved with global optimization, while Huygens's equivalent model is constructed in full-wave simulation tool.

With equivalent noise source model, the near-field coupling between radiation noise source and RF antennas are estimated by either direct simulation or reciprocity theorem. Field data is obtained by near-field scanning with phase information. Measurement data shows good correlation and consistence for noise source modeling and near-field coupling.

ACKNOWLEDGMENTS

This thesis represents not only my work at EMC lab since 2013, it is a result of all accumulative efforts made by all previous students, industrial colleagues and research professors for more than three years.

First and foremost I would like to thank my advisor, Prof. Jun Fan, director of the EMC lab. He has been supportive and willing to share his insights whenever I came across difficulties in research or life. The way Dr. Jun Fan treated research inspires me to be more independent in thoughts and more resourceful in solving problems. Since I began master study, Jun supported me by providing a research assistantship which allows me to concentrate more on research. I appreciate all these guidance and support that Jun offered. He is beyond the scope of academic advisor and also an exemplar of kindness and intelligence.

Thank you to Prof. David Pommerenke and Prof. Daryl Beetner for being my committee members. David is creative in coming up with refreshing ideas and helped me solve many tough measurement problems. His passion and dedication to research always reminds me to be proactive whatever I decide to do. Thank you to Daryl, with whom I worked with as Chair of the ECE department. His leadership skills and personal charisma impressed me since I met him. I sincerely express my gratitude for all he had done to help me through my master career.

Lastly, and most importantly, I wish to thank the people that loved me and gave me valuable suggestions. I am grateful to my parents who have been a constant source of love and support. To them I dedicate this thesis.

TABLE OF CONTENTS

LIST OF ILLUSTRATIONS

LIST OF TABLES

1. INTRODUCTION TO RIDIATION NOISE SOURCE MODELING

1.1. EQUIVALENT DIPOLE MOMENT MODEL

With increasing complexities of modern electronic systems, the electromagnetic interference issues are arising enormously. RF-digital mixed circuit design is the key to the system sensitivity and functional performance. Among electromagnetic interference problems, RF interference has much lower noise coupling level as stated in [1]. Since RF antennas have very high sensitivity, even small amount of noise that can be seen by the antenna will cause desensitization problem. A near-field noise coupling estimation technique is therefore expected to predict the coupling during pre-design process or guide the design for noise coupling mitigation [2]. In order to estimate the near-field noise coupling from digital module to RF components, the noise source is anticipated to be replaced by its equivalent radiation model which can facilitate the near-field coupling analysis.

Radiation noise source modeling is the key to estimating the near-field coupling in RF interference analysis. This thesis presents two methods for modeling radiation noise source and applying them to near-field coupling estimation. The noise source can be either modeled by physics-based dipole moment model or Huygens's equivalent model with data obtained from near-field scanning. The fundamental principles of both methods are first studied and compared by simulation. Later a clock buffer IC is used to demonstrate the application of dipole moment model to real measurement environment. The working IC is modeled as dipole moment model and the tangential fields on a Huygens's box can be calculated by dipole moment model of the IC with negligible multiple scattering effect assumption.

With equivalent radiation noise source model, the coupling then can be obtained by surface integration of Poynting vector at the RF antenna receiving port by full-wave simulation. In some cases, full-wave simulation of the radiator is difficult if not impossible. Another more comprehensive method based on Reciprocity Theorem is then proposed and capable to estimate the noise coupling without full-wave simulation [3][4]. Both methods are analyzed using simulation and measurement data and show good correlation.

1.1.1. Physical Foundations and Mathematical Derivation. In Cartesian coordinate system, based on the multipole expansion of a radiating source, any arbitrary electrically small source can be approximately replaced by six dipoles: three electric dipoles along x, y, z direction and three magnetic dipoles along x, y, z direction, which are denoted as P_x, P_y, P_z and M_x, M_y, M_z respectively [2][5]. The fields generated by the dipole sets are equivalent as that by the real source. With proper division, the volume occupied by the radiation source can be cut into several electrically small volume and further replaced by the electric and magnetic dipole sets.

As shown in Fig. 1.1, assume there are n dipole sets locating on an infinitely large ground plane and there are m observation points, the observed tangential E and H fields at each observation point can be calculated using equation (1) through (4) with superposition.
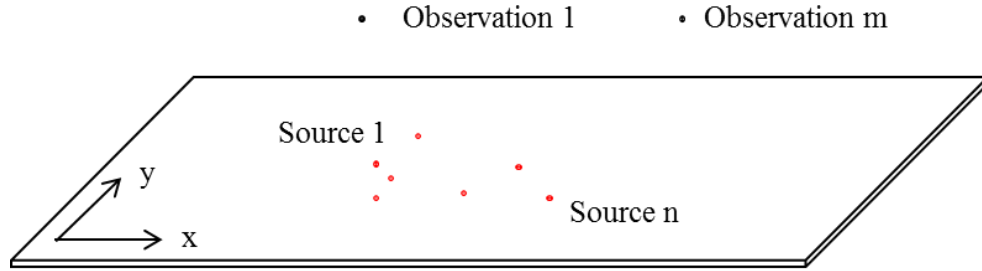
Figure 1.1. Dipole sets and observation points above ground plane

The tangential E and H field radiated by P_z, M_x and M_y dipoles can be written similar as in [6][8].

$$E_x = -j\frac{k_0\eta_0}{4\pi}\left\{\left[\frac{(z-h)(x-x')}{r_1^2}q_1(r_1)+\frac{(z+h)(x-x')}{r_2^2}q_1(r_2)\right]P_z \right.$$
$$\left. +\left[\frac{(z-h)}{r_1}q_3(r_1)+\frac{(z+h)}{r_2}q_3(r_2)\right]k_0M_y\right\}$$

$$(1)$$

$$E_y = -j\frac{k_0\eta_0}{4\pi}\left\{\left[\frac{(z-h)(y-y')}{r_1^2}q_1(r_1)+\frac{(z+h)(y-y')}{r_2^2}q_1(r_2)\right]P_z \right.$$
$$\left. +\left[-\frac{(z-h)}{r_1}q_3(r_1)-\frac{(z+h)}{r_2}q_3(r_2)\right]k_0M_x\right\}$$

$$(2)$$

$$H_x = \frac{k_0}{4\pi}\left\{ -\left[\frac{(y-y')}{r_1}q_3(r_1) + \frac{(y-y')}{r_2}q_3(r_2)\right]P_z\right.$$

$$+\left[-\frac{(y-y')^2+(z-h)^2}{r_1^2}q_1(r_1)+q_2(r_1) - \frac{(y-y')^2+(z+h)^2}{r_2^2}q_1(r_2)+q_2(r_2)\right]k_0 M_x$$

$$\left.+\left[\frac{(x-x')(y-y')}{r_1^2}q_1(r_1)+\frac{(x-x')(y-y')}{r_2^2}q_1(r_2)\right]k_0 M_y\right\}$$

(3)

$$H_y = \frac{k_0}{4\pi}\left\{ \left[\frac{(x-x')}{r_1}q_3(r_1) + \frac{(x-x')}{r_2}q_3(r_2)\right]P_z\right.$$

$$+\left[-\frac{(x-x')^2+(z-h)^2}{r_1^2}q_1(r_1)+q_2(r_1) - \frac{(x-x')^2+(z+h)^2}{r_2^2}q_1(r_2)+q_2(r_2)\right]k_0 M_y$$

$$\left.+\left[\frac{(x-x')(y-y')}{r_1^2}q_1(r_1)+\frac{(x-x')(y-y')}{r_2^2}q_1(r_2)\right]k_0 M_x\right\}$$

(4)

Where k_0 is the free space wave number, η_0 is the wave impedance in vacuum; P_z is a complex number denoting the electrical dipole along z direction with unit of $A \cdot m$; M_x and M_y denote the magnetic current along x and y direction respectively with unit of $A \cdot m^2$.

$$r_1 = \left[(x-x')^2 + (y-y')^2 + (z-h)^2\right]^{1/2}$$

(5)

$$r_2 = \left[(x-x')^2 + (y-y')^2 + (z+h)^2\right]^{1/2}$$

(6)

$$q_1(r) = \left[\frac{3}{(k_0 r)^2} + j\frac{3}{k_0 r} - 1\right]g(r)$$

(7)

$$q_2(r) = \left[\frac{2}{(k_0 r)^2} + j\frac{2}{k_0 r}\right]g(r)$$

(8)

$$q_3(r) = \left[\frac{1}{k_0 r} + j\right]g(r)$$

(9)

$$g(r) = \frac{e^{-jk_0 r}}{r}$$

(10)

It is worth mention that the dipole moment model takes the infinite large ground plane into account which results in the image terms in equation (1) through (4). In real

measurement, the PCB ground size is limited, so the multiple scattering between the source and the ground plane is included in the total scanned field. In this case, the dipole moment model represents the source only without the ground plane [8]. Based on image theory in [9], the image of electric/magnetic dipole in normal/tangential direction of perfect electric conductor has the same magnitude and direction as original electric/magnetic dipole; the image of electric/magnetic dipole in tangential/normal direction of perfect electric conductor has the same magnitude but opposite direction as original electric/magnetic dipole as shown in Fig. 1.2.
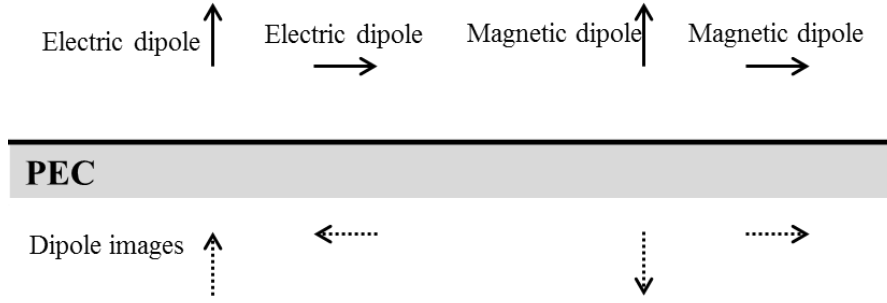
Figure 1.2. Image theory with infinite PEC plane

In most cases, the radiation source will be locating close to the ground (GND) plane which can be deemed as Perfect Electric Conductor (PEC). Hence the total contribution of vertical magnetic dipole and its image will be cancelled each other. Similarly, the tangential electric dipole and their images will cancel each other. In this study, P_z, M_x and M_y dipoles dominate and will only be used in the equivalent model for most cases. It can be seen from equation (1) through (4) that the observed field E and H are linearly dependent on the complex variable P_z, M_x and M_y. To be more intuitive, equation (1) through (4) can be written as a simple linear equation as equation (11) to equation (14).

$$E_x = T_{E_x\_P_z} \cdot P_z + 0 \cdot M_x + T_{E_x\_M_y} \cdot M_y \tag{11}$$

$$E_y = T_{E_y\_P_z} \cdot P_z + T_{E_y\_M_x} \cdot M_x + 0 \cdot M_y \tag{12}$$

$$H_x = T_{H_x\_P_z} \cdot P_z + T_{H_x\_M_x} \cdot M_x + T_{H_x\_M_y} \cdot M_y \tag{13}$$

$$H_y = T_{H_y\_P_z} \cdot P_z + T_{H_y\_M_x} \cdot M_x + T_{H_y\_M_y} \cdot M_y \tag{14}$$

Where $T_{E_x\_P_z}$, $T_{E_x\_M_y}$; $T_{E_y\_P_z}$, $T_{E_y\_M_x}$; $T_{H_x\_P_z}$, $T_{H_x\_M_x}$, $T_{H_x\_M_y}$; $T_{H_y\_P_z}$, $T_{H_y\_M_x}$ and $T_{H_y\_M_y}$

denote the transfer coefficient of field components that respect to different dipole types. For example, the transfer coefficient of E_x respects to P_z and M_y can be expressed as,

$$T_{E_x\_P_z} = -j\frac{k_0\eta_0}{4\pi}\left[\frac{(z-h)(x-x')}{r_1^2}q_1(r_1) + \frac{(z+h)(x-x')}{r_2^2}q_1(r_2)\right]$$

(15)

$$T_{E_x\_M_y} = -j\frac{k_0^2\eta_0}{4\pi}\left[\frac{(z-h)}{r_1}q_3(r_1) + \frac{(z+h)}{r_2}q_3(r_2)\right]$$

(16)

It can be observed that the transfer coefficients are related to frequency, source location, observation location, dipole type, dipole orientation for each individual dipole set. Further, equation (11) through (14) can be represented using matrix form as

$$\begin{bmatrix} E_x \\ E_y \\ H_x \\ H_y \end{bmatrix} = \begin{bmatrix} T_{E_x\_P_z} & 0 & T_{E_x\_M_y} \\ T_{E_y\_P_z} & T_{E_y\_M_x} & 0 \\ T_{H_x\_P_z} & T_{H_x\_M_x} & T_{H_x\_M_y} \\ T_{H_y\_P_z} & T_{H_y\_M_x} & T_{H_y\_M_y} \end{bmatrix} \begin{bmatrix} P_z \\ M_x \\ M_y \end{bmatrix}$$

(17)

Consider all the observation points on the scanning plane and dipole array. The tangential field on the scanning plane can be expressed in terms of the dipole moment multiplied by a transfer function using vectorization concept. In general, the relationship between observed field and dipole source can be written as a normal equation denoted as

$$Tx = F$$

(18)

Where T is the transfer matrix, x is unknown complex number that represents P_z, M_x and M_y with magnitude and phase information. Each of the elements in equation (18) can be decomposed in top-down sense. Concretely, the field F can be decomposed as electrical field and magnetic field. The unknown is the magnitude and phase of dipole sets. Transfer matrix T can be expressed as sub-matrixes that connect source and victim.

$$F = \begin{bmatrix} E \\ H \end{bmatrix} = \begin{bmatrix} E_x \\ E_y \\ E_z \\ H_x \\ H_y \\ H_z \end{bmatrix} = \begin{bmatrix} \begin{bmatrix} E_{x1} \\ ... \\ E_{xm} \end{bmatrix} \\ E_y \\ ... \\ H_z \end{bmatrix}$$

(19)

$$x = \begin{bmatrix} P \\ M \end{bmatrix} = \begin{bmatrix} \begin{bmatrix} P_1 \\ M_1 \end{bmatrix} \\ ... \\ \begin{bmatrix} P_n \\ M_n \end{bmatrix} \end{bmatrix} = \begin{bmatrix} \begin{bmatrix} P_{x1} \\ P_{y1} \\ P_{z1} \\ M_{x1} \\ M_{y1} \\ M_{z1} \end{bmatrix} \\ ... \\ \begin{bmatrix} P_n \\ M_n \end{bmatrix} \end{bmatrix}$$

(20)

$$T = \begin{bmatrix} T_1 ... T_n \end{bmatrix} = \begin{bmatrix} T_{(EH)\_(PM)_1} ... T_{(EH)\_(PM)_n} \end{bmatrix} = \begin{bmatrix} T_{E\_(PM)_1} ... T_{E\_(PM)_n} \\ T_{H\_(PM)_1} ... T_{H\_(PM)_n} \end{bmatrix}$$

$$= \begin{bmatrix} \begin{bmatrix} T_{E_x\_(PM)_1} ... T_{E_x\_(PM)_n} \\ T_{E_y\_(PM)_1} ... T_{E_y\_(PM)_n} \\ T_{E_z\_(PM)_1} ... T_{E_z\_(PM)_n} \end{bmatrix} \\ ... \\ T_{H\_(PM)_1} ... T_{H\_(PM)_n} \end{bmatrix} = \begin{bmatrix} \begin{bmatrix} \begin{bmatrix} T_{E_{x1}\_(PM)_1} ... T_{E_{x1}\_(PM)_n} \\ ... \\ T_{E_{xm}\_(PM)_1} ... T_{E_{xm}\_(PM)_n} \end{bmatrix} \\ T_{E_y\_(PM)_1} ... T_{E_y\_(PM)_n} \\ T_{E_z\_(PM)_1} ... T_{E_z\_(PM)_n} \end{bmatrix} \\ ... \\ T_{H\_(PM)_1} ... T_{H\_(PM)_n} \end{bmatrix}$$

$$= \begin{bmatrix} \begin{bmatrix} \begin{bmatrix} T_{E_{x1}-P_{x1}} & T_{E_{x1}-P_{y1}} & T_{E_{x1}-P_{z1}} & T_{E_{x1}-M_{x1}} & T_{E_{x1}-M_{y1}} & T_{E_{x1}-M_{z1}} \end{bmatrix} \cdots T_{E_{x1}-(PM)_n} \\ \cdots \\ T_{E_{xm}-(PM)_1} \cdots T_{E_{xm}-(PM)_n} \end{bmatrix} \\ T_{E_y-(PM)_1} \cdots T_{E_y-(PM)_n} \\ T_{E_z-(PM)_1} \cdots T_{E_z-(PM)_n} \\ \\ \cdots \\ T_{H-(PM)_1} \cdots T_{H-(PM)_n} \end{bmatrix} \tag{21}$$

Generally, if there are m observation points and n dipole sets, F will be a $3m \times 1$ dimensional vector and x is a $6n \times 1$ dimensional vector. T will be a $3m \times 6n$ dimensional matrix. Note that the transfer matrix is not only dependent on frequency, source location, observation location, dipole type, dipole orientation, but also dependent on number of dipoles since it describes a group of dipole sets. Also the number of dipole is coupled to the source location. Equation (19) through (21) are complete and general equations that consider all field components and dipole types. In most applications later in this thesis, the dipole type is limited to P_z, M_x and M_y. The field will be limited to magnetic field only.

1.1.2. Model Extraction. Usually, the number of scanning points m will be much greater than two times of the number of dipole sets, i.e. the number of rows will be much greater than the number of columns for matrix T ($3m \gg 6n$), which results in an "over-determined" system. Mathematically, the number of equations is greater than unknowns in which case there is no solution to the equation unless all measurements are perfect [10]. In real measurement cases, the error $e = F - T \cdot x$ always exists. When the Euclidean length of e is minimum, $\hat{x}$ is called the least square solution to equation $Tx = F$. The Euclidean length of e can be expressed as

$$e = \|Tx - F\|^2 \tag{22}$$

The solution $\hat{x}$ can be demonstrated to be expressed as

$$Tx = F \Rightarrow T'Tx = T'F \Rightarrow x = (T'T)^{-1}T'F \tag{23}$$

Where T' denotes the conjugate transpose of T. In this inverse problem, usually the matrix T is ill-posed since the number of rows is greater than the number of columns and measurement data always contain noise. In this case, the solution to equation (18) will be sensitive to small disturbance of both T and F. Normalization is found to result in a better matrix condition number and therefore a more accurate solution to the equation based on [6]. Consider the magnetic field radiated by P_z, M_x and M_y dipoles,

$$\begin{bmatrix} [H_x]_{m\times1} \\ [H_y]_{m\times1} \end{bmatrix} = \begin{bmatrix} T_{Hx\_Pz} & T_{Hx\_Mx} & T_{Hx\_My} \\ T_{Hy\_Pz} & T_{Hy\_Mx} & T_{Hy\_My} \end{bmatrix} \begin{bmatrix} [P_z]_{n\times1} \\ [M_x]_{n\times1} \\ [M_y]_{n\times1} \end{bmatrix}$$

(24)

First, the magnetic field data is normalized as

$$F_n = \begin{bmatrix} [H_x]_{m\times1}/H_{max} \\ [H_y]_{m\times1}/H_{max} \end{bmatrix}$$

(25)

In which H_{max} is the maximum magnitude of the tangential H fields. The equivalent dipole moments are also normalized as

$$X_n = \begin{bmatrix} [P_z]_{n\times1} \\ [k_0 M_x]_{n\times1} \\ [k_0 M_y]_{n\times1} \end{bmatrix}$$

(26)

Where X_n denotes the normalized dipole moments. Substituting (25) and (26) into (24) yields the normalized transfer matrix T_n

$$T_n = \begin{bmatrix} T_{Hx\_Pz}/H_{max} & T_{Hx\_Mx}/(H_{max}k_0) & T_{Hx\_My}/(H_{max}k_0) \\ T_{Hy\_Pz}/H_{max} & T_{Hy\_Mx}/(H_{max}k_0) & T_{Hy\_My}/(H_{max}k_0) \end{bmatrix}$$

(27)

By linear least-square method, the normalized solution X_n can be calculated as

$$X_n = [T_n'T_n]^{-1} T_n'F_n$$

(28)

If the number of features is excessively large, i.e. the number of dipoles is large, overfitting problem will arise. To address this issue, regularization or Singular Value Decomposition is incorporated to mitigate it. The main idea of regularization is to

minimize the norm (a.k.a Euclidean distance) of e and minimize total energy of the dipole sets. The objective function for searching optimal x can be written as

$$e_{reg} = \|F_n - T_n X_n\|^2 + \lambda^2 \|X_n\|^2 \tag{29}$$

Where λ is a regularization coefficient, the first term $\|F_n - T_n X_n\|^2$ in e_{reg} determines the accuracy of solution X_n and the second term $\lambda^2 \|X_n\|^2$ determines the total energy of unknown dipole sets. The regularized least-square solution that minimizes equation (29) can be written as

$$X_n = [T_n' \cdot T + \lambda^2 I]^{-1} \cdot T_n' F_n \tag{30}$$

If λ is zero, the objective function will be the same case that without regularization. Increasing λ will result in larger error (larger penalty) for objective function. The least square algorithm will therefore try to minimize the second term which is the total energy of dipole sets. However, λ cannot be too large otherwise the accuracy term will have little impact on the objective function that will cause under fitting problem.

      1.1.3. Simulation Validation. The dipole moment model extracted using least square method is validated by simulation with a patch antenna case. The patch antenna is locating on a 200 mm by 200 mm ground plane as shown in Fig. 1.3. The length along x direction is 37.2 mm, and width along y direction is 28 mm. The solution frequency is 2.4 GHz in HFSS [7] and observation plane is at 5 mm above patch antenna. And field on z = 10 mm plane is used to validate the prediction of equivalent dipole moment model.
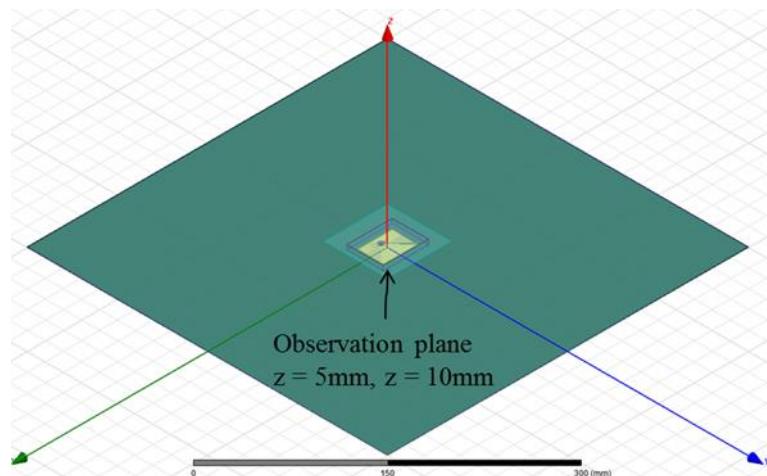
Figure 1.3. Patch antenna model in HFSS

The tangential E and H field pattern on z = 5 mm and z = 10 mm is shown in Fig. 1.4 from HFSS simulation which is used for dipole model extraction and prediction respectively.
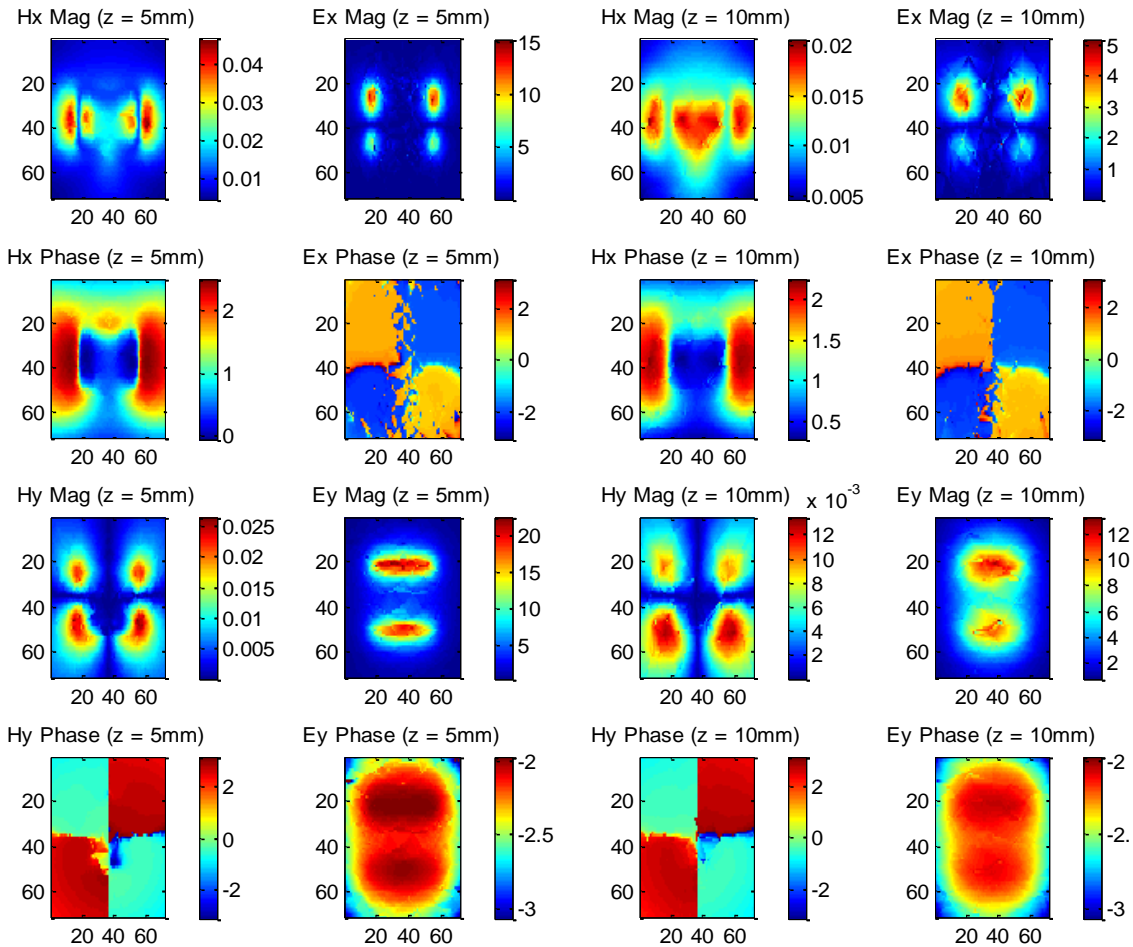
Figure 1.4. Tangential E and H field pattern at z = 5 mm and 10 mm from simulation of original patch antenna

First, only tangential H field data is used to extract the equivalent dipole moment model. The observation plane at z = 5 mm with dimension 70 mm by 70 mm and spacing equals to 1 mm. The dipole sets are uniformly distributed at z = 1 mm plane. There are 9 rows and 8 columns of dipoles along x direction and y direction respectively as shown in Fig. 1.5. The blue dots on top represent the observation points and red dots at the bottom represent the dipole sets.
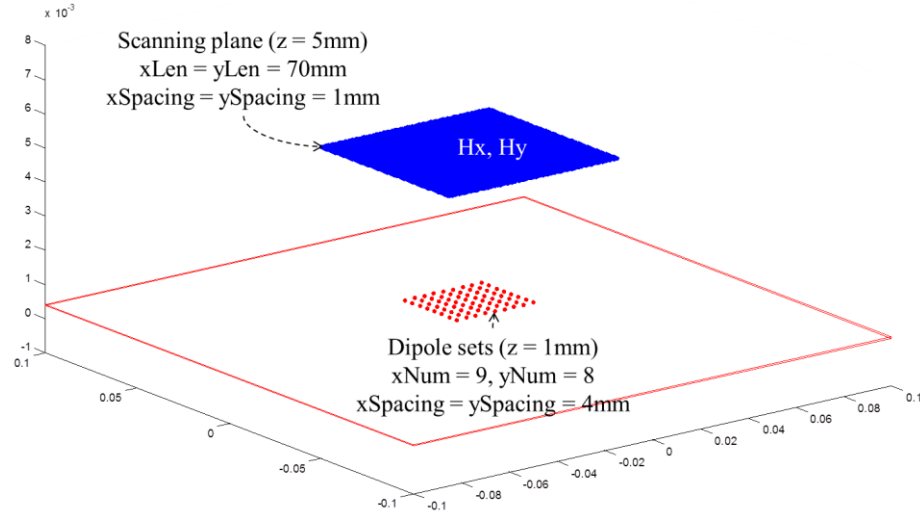
Figure 1.5. Configuration of observation plane (H only) and dipole moment sets

Based on the extraction method described above, the field pattern at the observation plane z = 5 mm can be fitted by least square method and the field pattern at z = 10 mm can be predicted using the extracted dipole moment model as shown in Fig. 1.6.
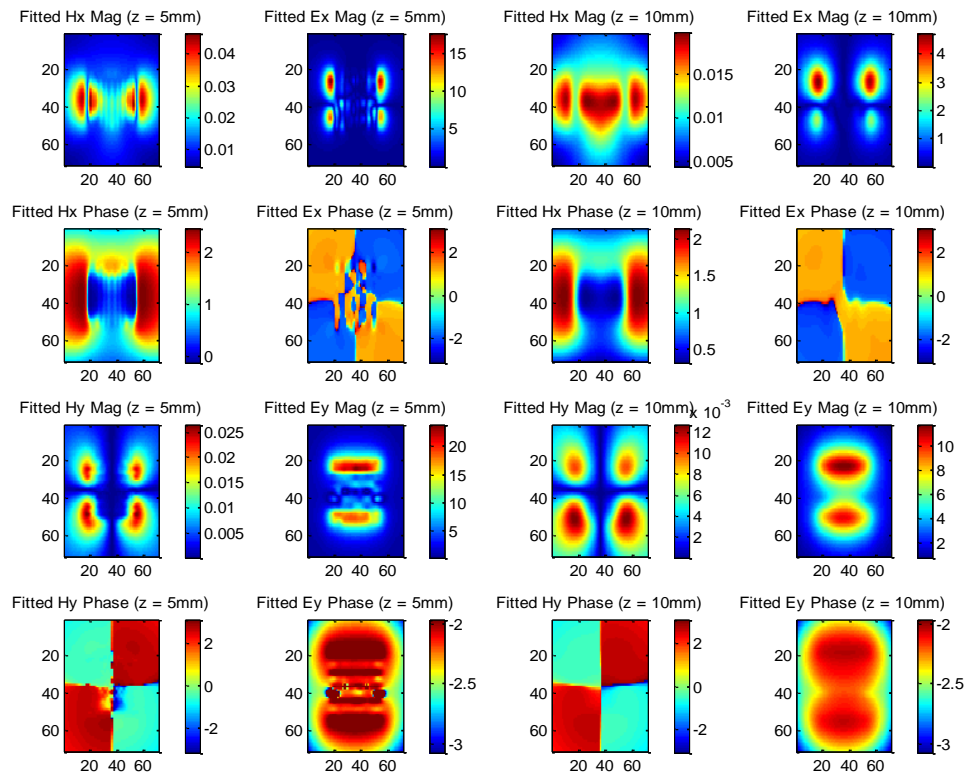
Figure 1.6. Tangential E and H field pattern at z = 5 mm and 10 mm from calculation of equivalent dipole moment model (extracted by H only)

It can be seen from the comparison between tangential E and H field pattern is agreed well with minor discrepancies. The field pattern is reconstructed by equivalent dipole moment at z = 5 mm and well predicted at other plane with z = 10 mm. In this part, only tangential H field data is used. In order to investigate if using only tangential H field data is enough to extract the dipole moment model; the later part introduces using both tangential E and H field data to extract the equivalent dipole moment with same simulation configuration and dipole configuration as shown in Fig. 1.7.
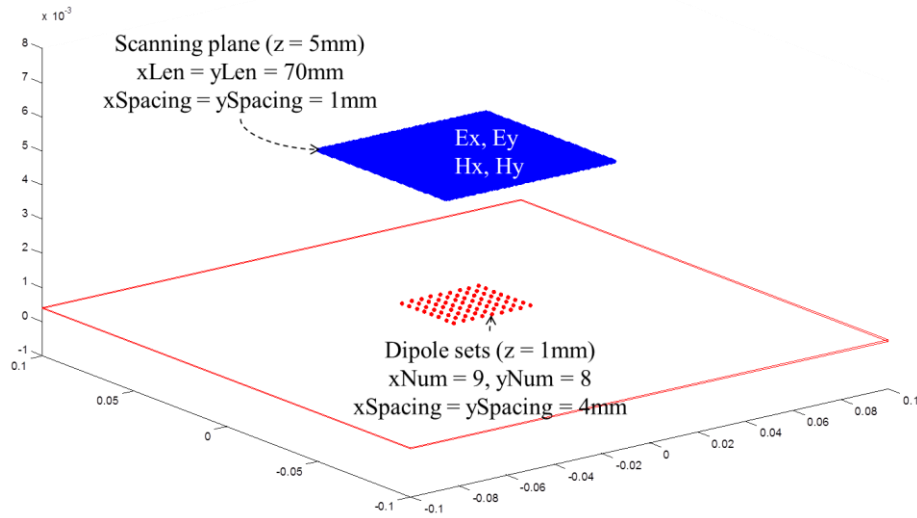
Figure 1.7. Configuration of observation plane (E and H) and dipole moment sets

The simulated field pattern is the same as Fig. 1.4, while the fitted field pattern will be different since equation (19) includes tangential E field as well which can written as

$$
F = \begin{bmatrix} [E] \\ [H] \end{bmatrix} = \begin{bmatrix} [E_x] \\ [E_y] \\ [H_x] \\ [H_y] \end{bmatrix} = \begin{bmatrix} \begin{bmatrix} E_{x1} \\ ... \\ E_{xm} \end{bmatrix} \\ [E_y] \\ [H_x] \\ [H_y] \end{bmatrix}
\tag{31}
$$

The dipole sets configuration is the same as that in the case where only H field is used. The only difference is that both tangential E and H field are used to extract the equivalent dipole model. Similarly, the tangential field pattern can be shown as in Fig. 1.8 below.
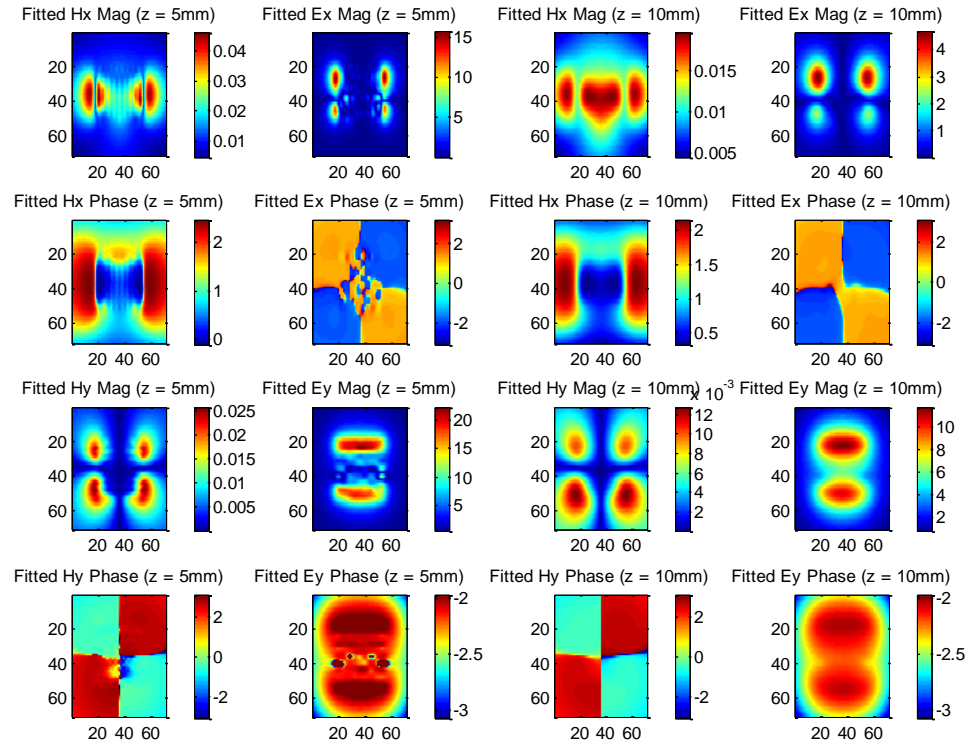
Figure 1.8. Tangential E and H field pattern at z = 5 mm and 10 mm from calculation of equivalent dipole moment model (extracted by E and H)

Comparing the fitted field pattern where only H field is used and both E and H field are used, it shows little difference between the two. The result may be slightly better due to more data points in vector F. So using only tangential H field can be as good as using both E and H field for dipole model extraction. This conclusion improves near-field scanning efficiency that only H field probe is needed and near-field scanning time will be reduced to half.

1.1.4. Measurement Validation. A test board with passive patch antennas and u-shape trace is measured to further validate the dipole moment model. The test board is shown in Fig. 1.9 with dimensions 220 mm by 160 mm. It is a two layer board with patch and trace thickness equals to 0.035 mm, FR-4 dielectric layer thickness equals to 1.58 mm, and the ground layer thickness equals to 0.035 mm. The patch is antenna is 28 mm by 37.2 mm working at 2.45 GHz resonant frequency. It is noted that both magnitude and phase information are required to solve equation (28). There are several phase measurement methods proposed in literature [11][12]. Since the all the structure

are passive antennas, using Vector Network Analyzer (VNA) to measure phase will be a good choice since it has good sensitivity and accurate phase.
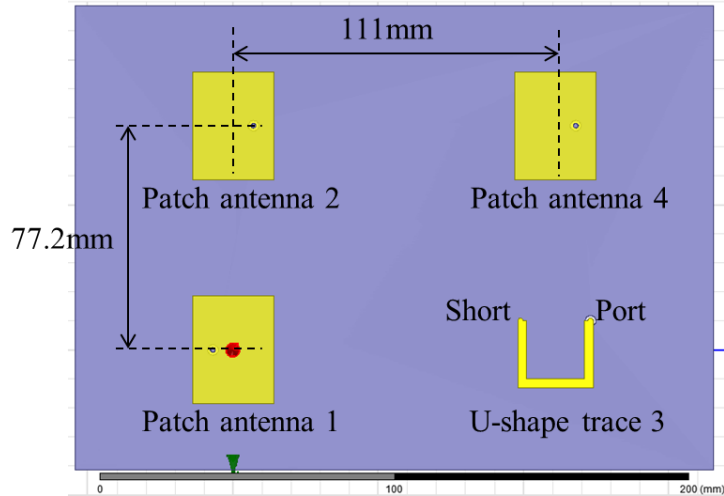
Figure 1.9. Test board with passive patch antennas and u-shape trace

In real measurement, only s-parameter can be measured. To obtain real H field, the s-parameter should be converted to H field by a complex factor which is defined as probe factor. Probe factor is calculated by probe calibration using a 50 ohm microstrip line whose diagram is shown as Fig. 1.10.
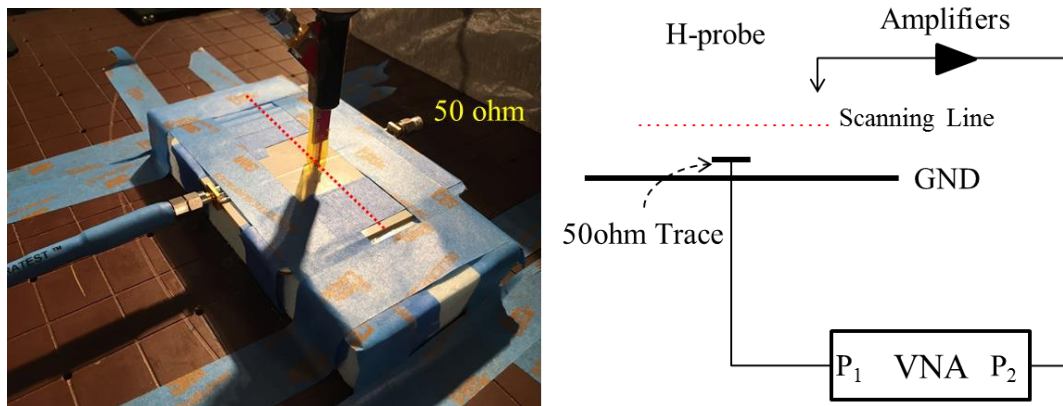
Figure 1.10. H-field calibration setup and diagram

The 50 ohm microstrip is also modeled in full-wave simulation tool to obtain the real H field data at the same location as points on the scanning line specified in Fig. 1.10 above. The simulation model is shown below in Fig. 1.11. In simulation, the same 50 ohm trace

board is simulated then obtains the H field component perpendicular to the trace direction.
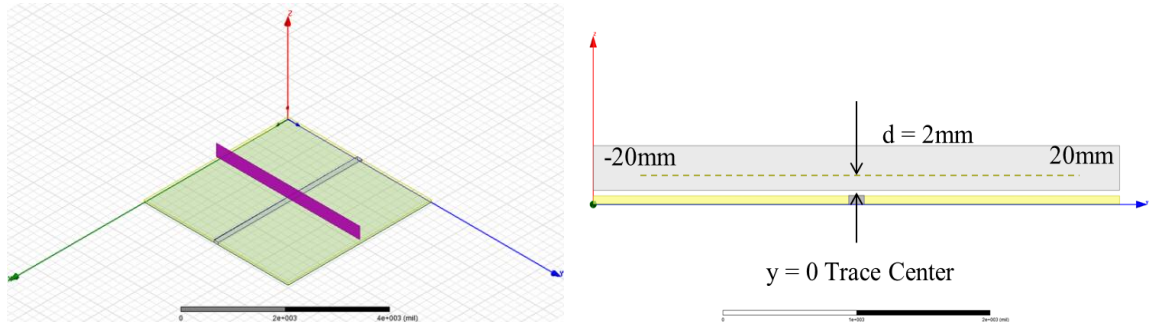
Figure 1.11. Simulation model of 50 ohm trace and observation line

By changing the height of scanning line in simulation, the 1D Hy field pattern will be different based on Ampere's law as shown in Fig. 1.12 and Fig. 1.13 The null points occur when the probe loop is parallel with the magnetic field line, and the distance between them increases when the observation height is increasing.
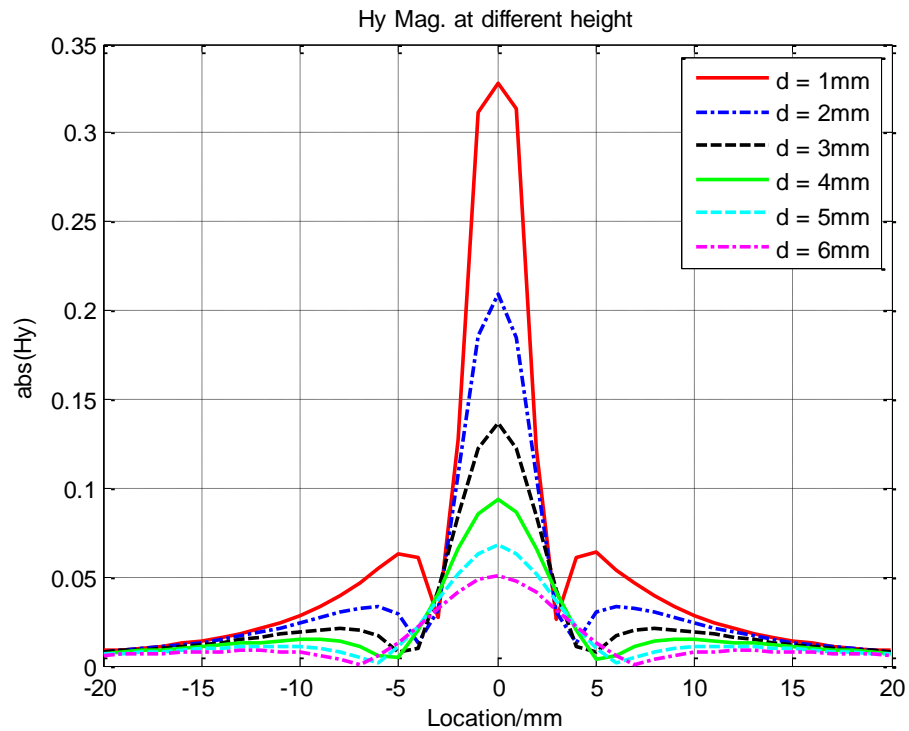
Figure 1.12. Hy magnitude pattern with different height above 50 ohm trace
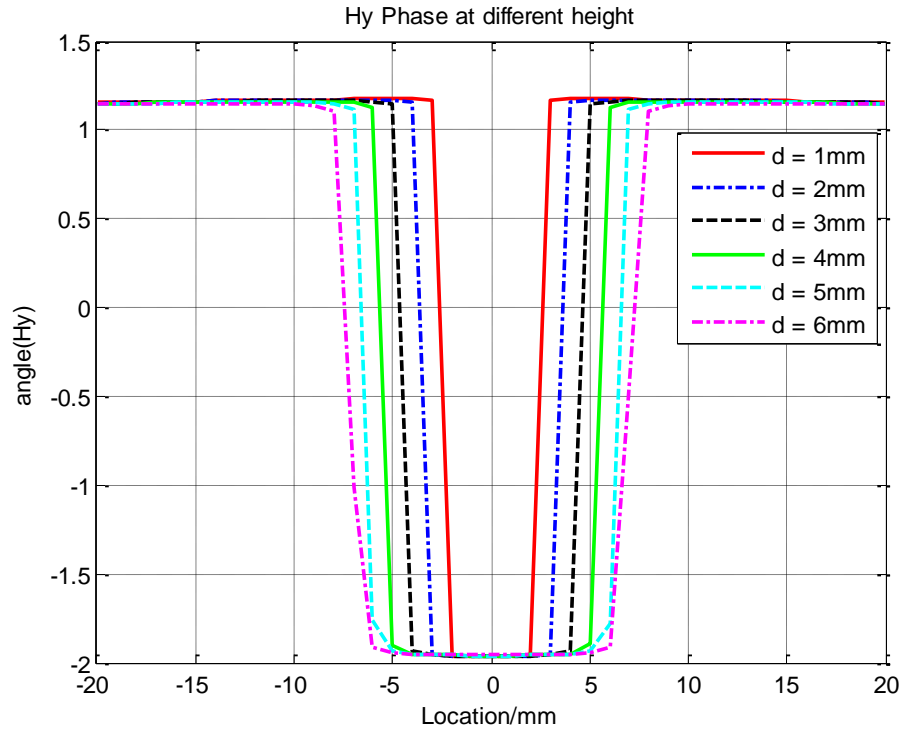
Figure 1.13. Hy phase pattern with different height above 50 ohm trace

The equivalent probing center of a real H field probe can be found by comparing the 1D Hy pattern between simulation and measurement as shown in Fig. 1.14 and Fig. 1.15. Both S-parameter and H field are linearly normalized as shown in equation (32).

$$x_n = \frac{x - \min(\min(x))}{\max(\max(x)) - \min(\min(x))} \tag{32}$$

It is found that when d = 4 mm in simulation, it matches well with measured S-parameter with height equals to 2 mm. So the equivalent height of probe center is 2 mm. The probe factor is defined as the ratio of simulated Hy and measured voltage. It should be noted that the amplifiers should work in linear region otherwise the probe factor will no longer be a linear relationship between simulated H field and measured voltage.

The main idea for using a 50 ohm matched trace to calibrate is that with different scanning height, the peak H field location is a function of the height, and the probe, cable etc. are linear system as shown in Fig. 1.16. By comparing the measurement and simulation data, the equivalent height of the probe can be obtained by comparing the measurement and simulation data.
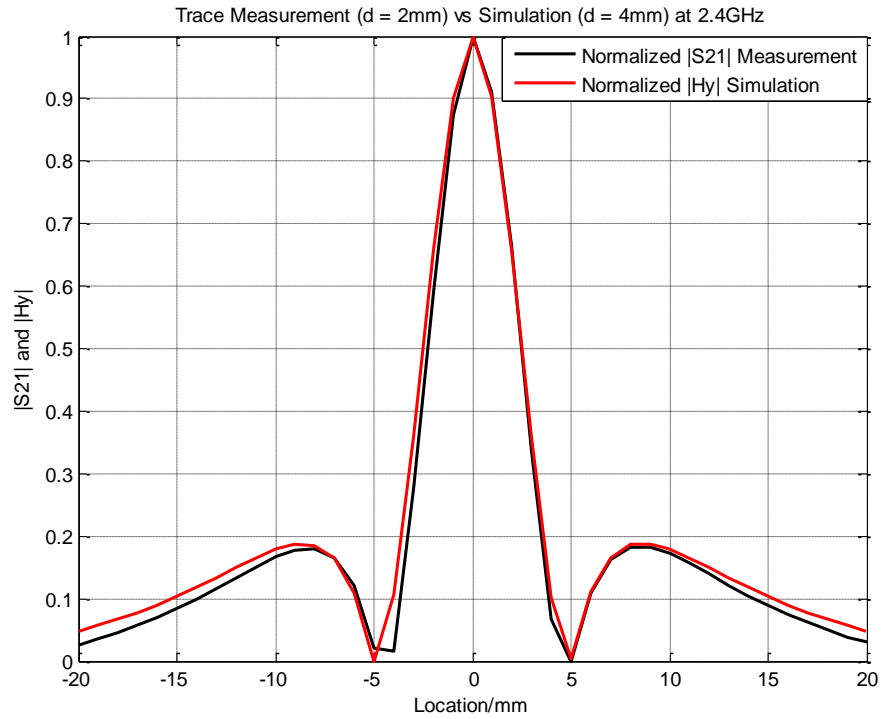
Figure 1.14. Comparison between normalized Hy and S21 magnitude pattern
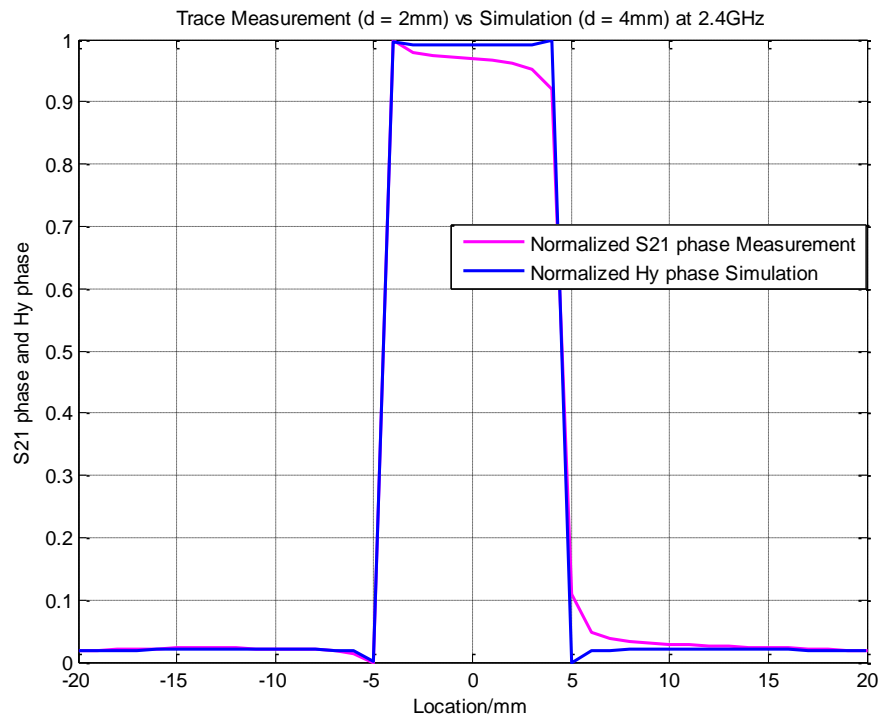
Figure 1.15. Comparison between normalized Hy and S21 phase pattern
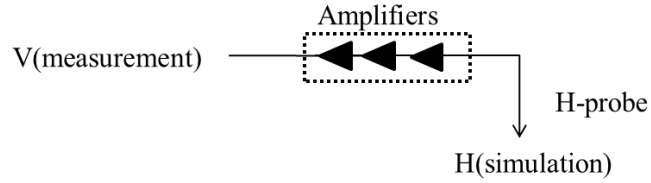
Figure 1.16. Linear-time-invariant system assumption for probing chain

$$PF = \frac{H_s}{V_m}\bigg|_{\text{at same location and frequency}} \tag{33}$$

H_s denotes simulated H field which is obtained at the same location as in near-field scanning. V_m is the measured voltage at the VNA port 2 which is equal to V_2^{ref} in equation (34). The relationship of H_s, S_{21}, P_{VNA_out} and PF can be expressed as equation (34), where S_{21} is total insertion loss measured by VNA, P_{VNA_out} is the power sent from VNA port 1.

$$
\left.
\begin{aligned}
P_{VNA\_out} &= 0dBm \\
S_{21} &= \frac{V_2^{ref}}{V_1^{inc}} \\
P_{VNA\_out} &= \frac{1}{2}\operatorname{Re}\{V_1^{inc} \cdot I_1^{inc}*\} = \frac{V_1^{inc2}}{100} \\
H_s &= V_2^{ref} \cdot PF
\end{aligned}
\right\}
\Rightarrow H_s = S_{21} \cdot 10 \cdot \sqrt{P_{VNA\_out}} \cdot PF \tag{34}
$$

With probe factor calculated, all later measured s-parameter can therefore be converted to real H field with the derivation above. With H field probe calibrated, the test board is scanned to obtain tangential H field data on a plane as shown below in Fig. 1.17.
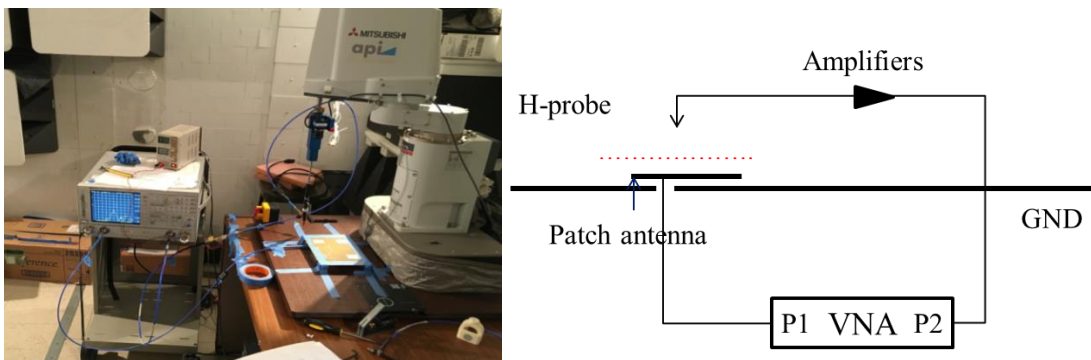
Figure 1.17. Measurement setup and overall diagram for test board validation

The scanning area is 70 mm by 70 mm with 1 mm step and the height is 2 mm above the patch. The VNA has 0 dBm output power, IF bandwidth is 1 kHz, and frequency range is 50 MHz to 5 GHz with 1601 points. Only tangential components are scanned and the raw S21 pattern at 2.4GHz is shown in Fig. 1.18.
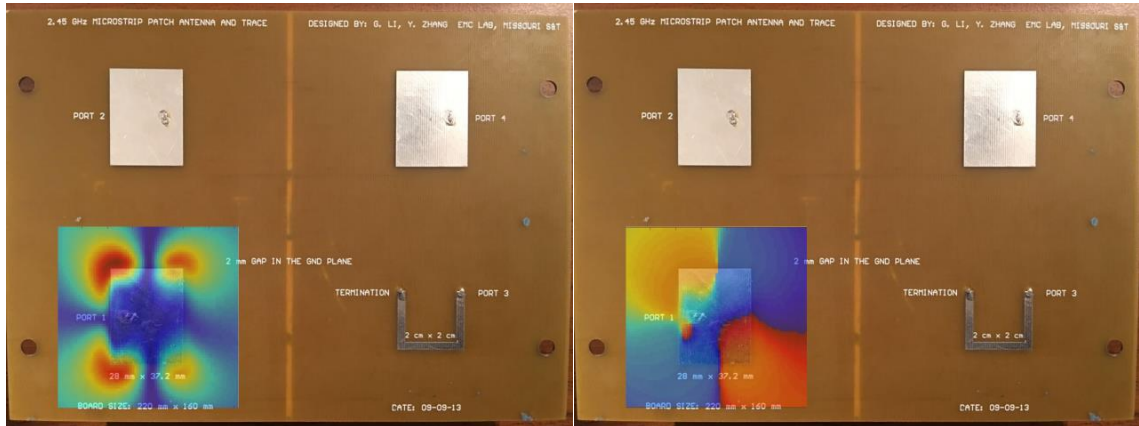
(a)   (b)
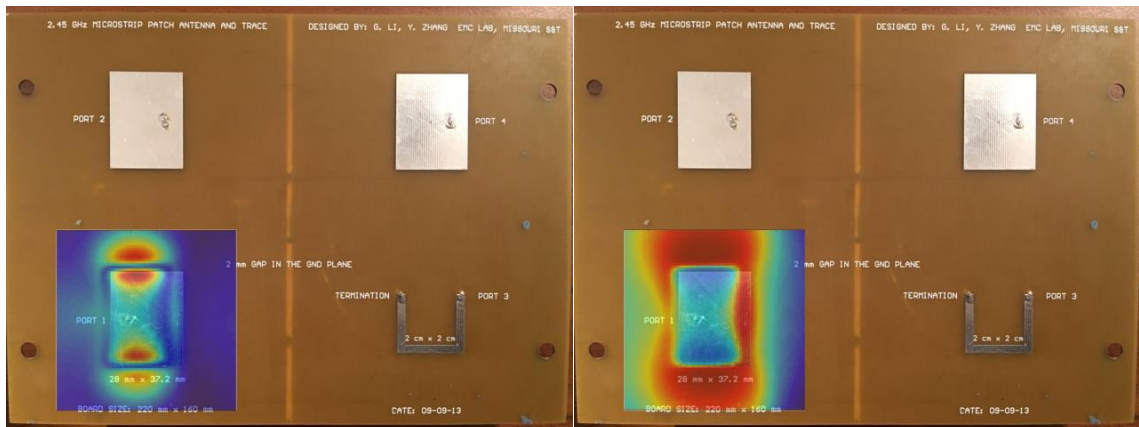
(c)   (d)

Figure 1.18. (a) Raw S21 magnitude along x direction; (b) Raw S21 phase along x direction; (c) Raw S21 magnitude along y direction; (d) Raw S21 phase along y direction

The pattern of raw s-parameter shows physical behavior of field distribution for a pattern antenna structure. The field at four corners are stronger than field in the center for x component and field at top and down sides are stronger than other sides for y component. Considering probe factor conversion, the H field pattern can be converted from s-parameter and is shown in Fig. 1.19. The tangential H field is converted by multiplying raw s-parameter with probe factor that is calibrated in the discussion above.
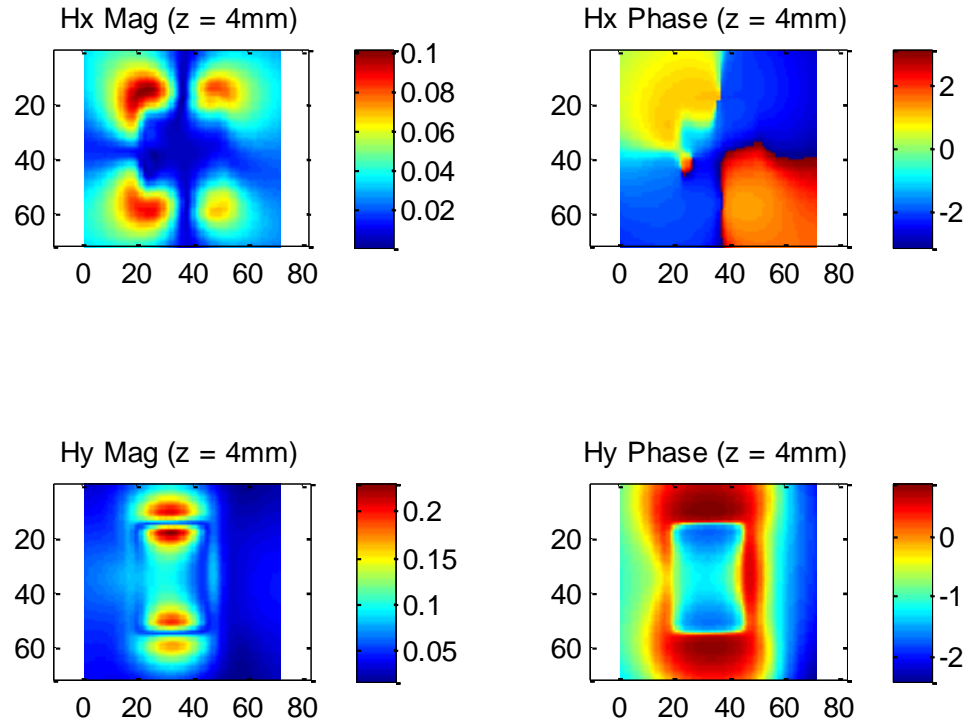
Figure 1.19. Real H field data converted from raw S21 by near-field scanning

At 2.4 GHz, the difference between raw S21 pattern and H field pattern is linear due to the definition of probe factor. In the meantime, the test board is simulated in full-wave simulation tool in HFSS as shown in Fig. 1.20.
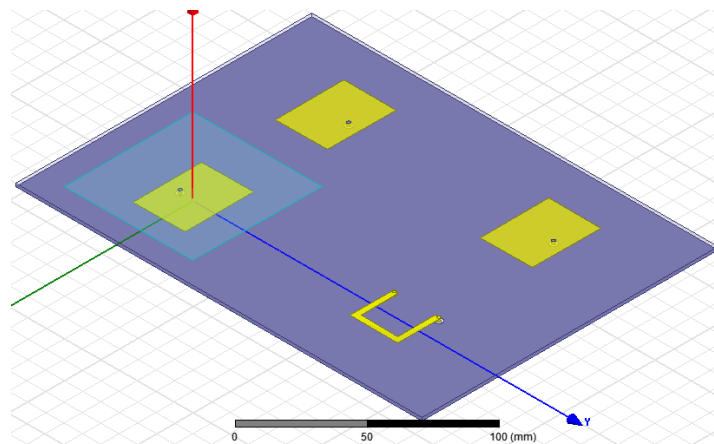
Figure 1.20. Full-wave simulation model of test board

In HFSS, the solution type is set as driven terminal with wave-port excitation at the patch antenna port.

The solution frequency is 2.4 GHz. The tangential H field at z = 4 mm plane is shown in Fig. 1.21.
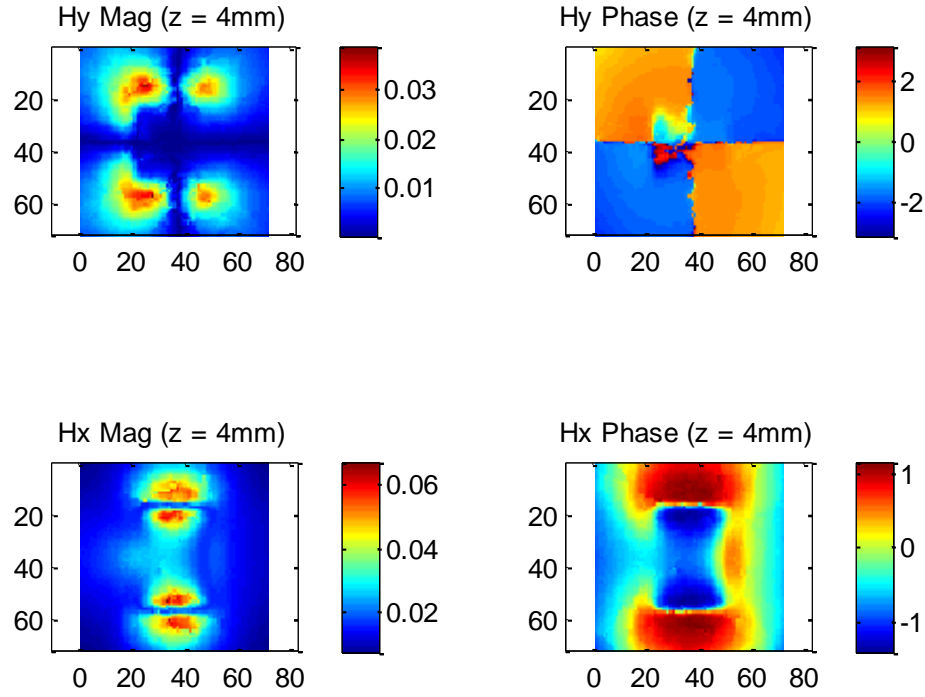
Figure 1.21. Real H field data by full-wave simulation

While there are some discrepancies between simulation pattern and measured pattern, the overall pattern agrees with each other. This implies the H field measurement is reasonable and phase measurement is good. With tangential H field data, the unknown dipole moment can be solved based on the discussion in Section 1.1.2. The initial dipole sets are specified as Fig. 1.22.
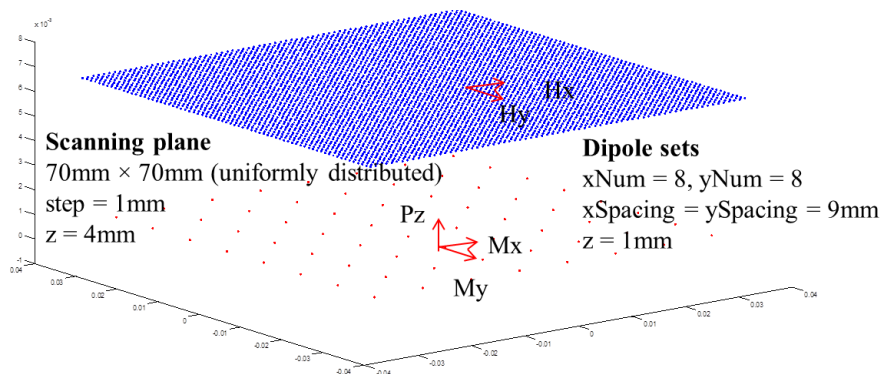
Figure 1.22. Near-field scanning points and dipole sets distribution

With equivalent dipole moment model of the patch antenna, theoretically the field at anywhere can be calculated. The field pattern at z = 10 mm is used to verify the accuracy of the extracted dipole model. There are three groups of data to validate the dipole model extraction method: A) measured tangential H field pattern at z = 10 mm; B) simulated tangential H field pattern at z = 10 mm; C) predicted tangential H field pattern at z = 10 mm. By comparing A) and C), the accuracy of dipole arrays can be validated. By comparing B) and C), the measurement accuracy can be verified. The measured tangential H field pattern at z = 10 mm is shown below in Fig. 1.23.
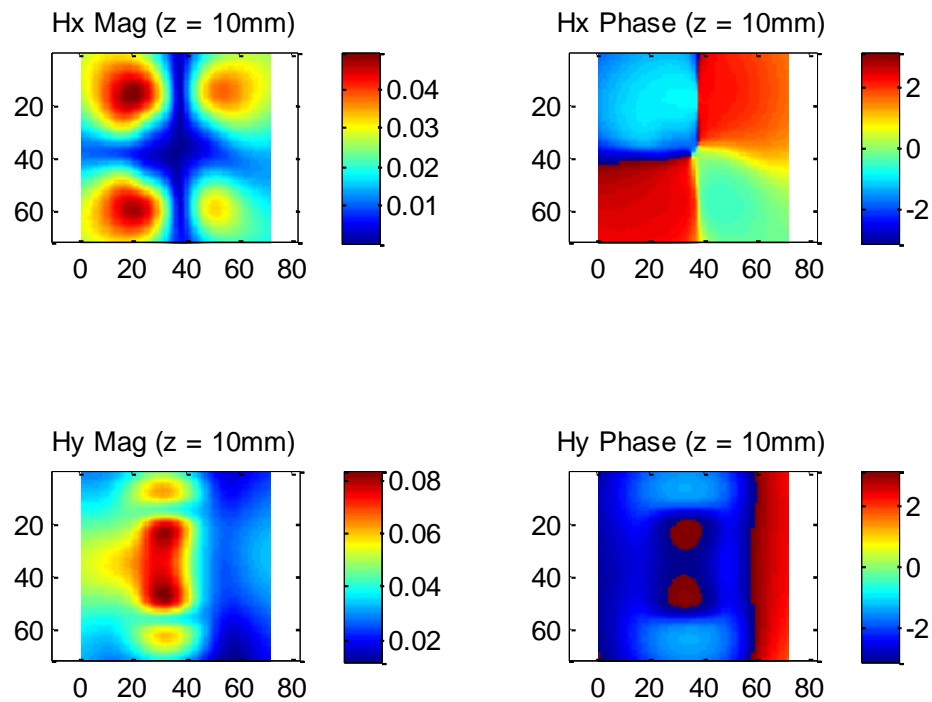
Figure 1.23. Tangential H field pattern at z = 10 mm plane by near-field scanning

The simulated H field pattern at z = 10mm is shown in Fig. 1.24. It can be seen from Fig. 1.23 and Fig. 1.24 that the tangential Hx and Hy field pattern is similar to each other. It indicates that the near-field scanning is consistent with simulation and the phase measurement method works well. The discrepancies of magnitude between simulation and measurement may be caused by the loss of connectors, reflections and instrument errors. With equivalent dipole moment model, the tangential H field pattern at z = 10 mm plane can be calculated analytically based on equation (24). The tangential H field pattern at z = 10 mm is shown in Fig. 1.25.
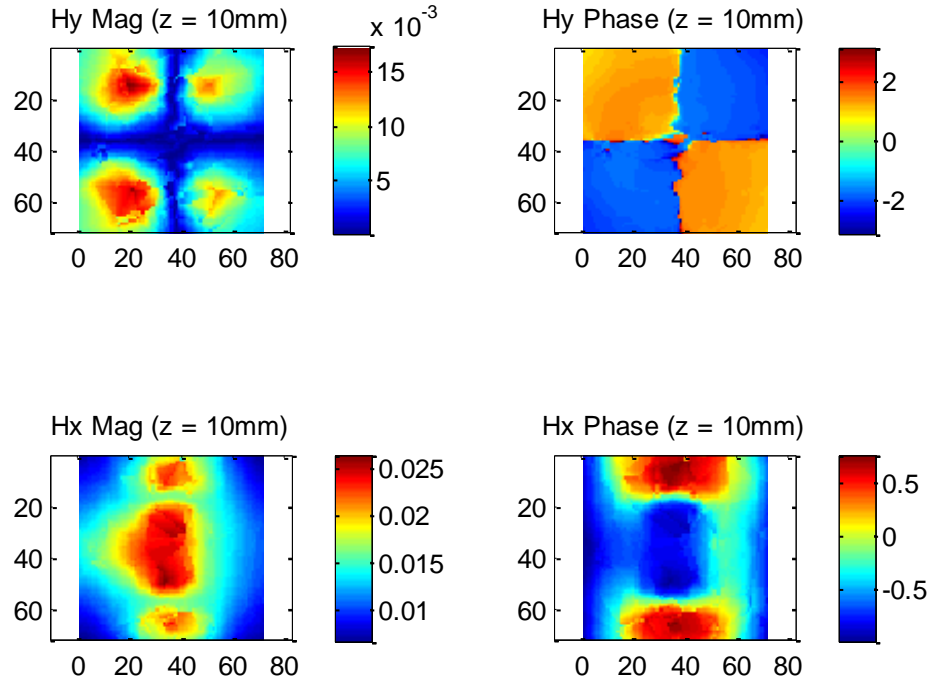
Figure 1.24. Tangential H field pattern at z = 10 mm plane by full-wave simulation

By comparing the magnitude and phase of Hx and Hy, the overall pattern is agreed between scanning and prediction.
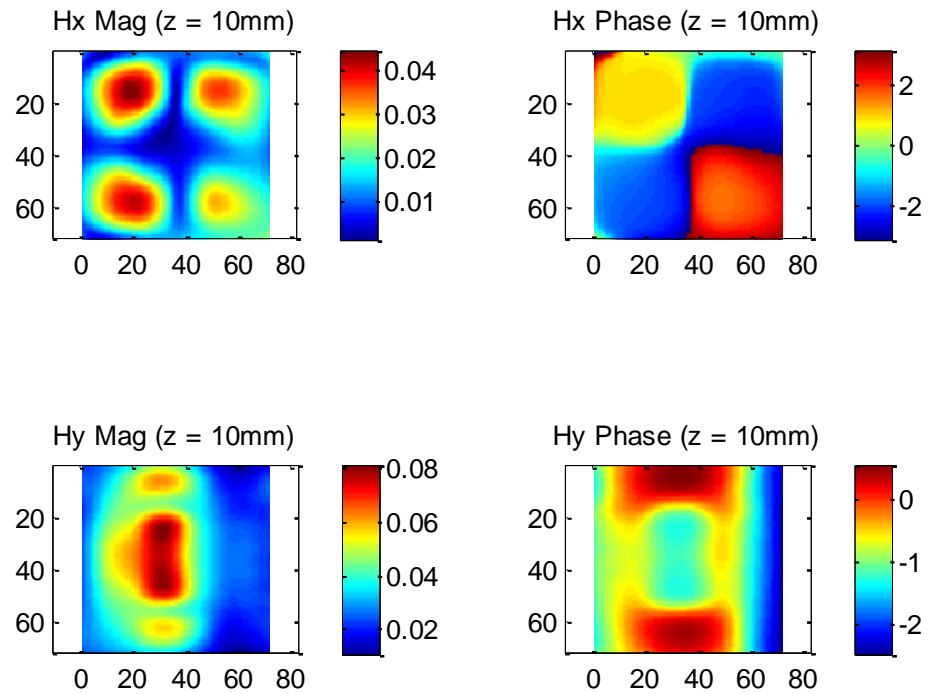
Figure 1.25. Tangential H field pattern at z = 10 mm plane by dipole moment model

It can be seen from the field patterns above that the measurement is consistent with simulation, the dipole moment model can be extracted with tangential H field only from z = 4 mm, and the equivalent model can predict the field at other locations.

1.1.5. Analysis and Optimization. It is worth mention that the dipole moment model takes the infinite large ground plane into account which results in the image terms in equation (1) (2). In real measurement, the PCB ground size is limited, so the multiple scattering between the source and the ground plane is included in the total scanned field. In this case, the dipole moment model represents the source only without the ground plane. Besides, the dipole type is limited to Pz, Mx and My due to images theory approximation. The approximation assumes the radiation source is right on the ground plane so that the Px, Py and Mz dipoles will get cancelled. In realty there is some space between the radiation source and ground plane, so using only Pz, Mx and My will be a close approximation. The transfer matrix T is dependent on location of observation points r , location of source points r' , frequency f and dipole type, dipole orientation and dipole number. While in real implementation as shown in Fig. 1.26,
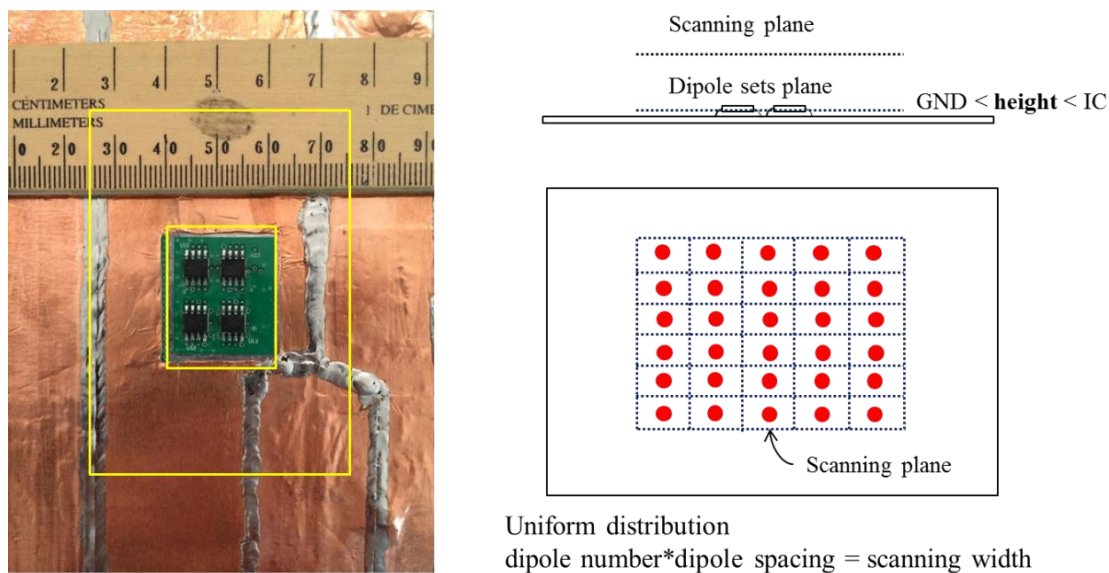
Figure 1.26. Dipole sets configuration for plain Least-square method

The radiation source is specified as a working clock IC array. To equivalently replace the radiation source, the dipole sets are pre-defined based on empirical rules: the

dipole sets are distributed uniformly on a plane locating higher than ground plane while lower than the IC array. The number of dipole times spacing of dipole equals to the scanning width, and the dipole spacing is usually in the range of $\lambda/20$ and $\lambda/10$. If the spacing is too small, the transfer matrix will be degenerated to a singular matrix and the solution will have large error. In order to get a good solution to the normal equation (18), some prior experience is required to place the dipole sets in a good pattern. This is one of the limitations of dipole moment model extraction due to no criteria to select dipole location, type, orientation and number.

　　　　To improve the algorithm, global optimization method is proposed. To address the dipole type and dipole orientation issue, all six dipole types are put along x, y and z directions, i.e. Px, Py, Pz, Mx, My and Mz. The magnitude and phase determines the weights of each dipole type and their orientation in the solution. The remaining unknown parameters is r' and dipole number. Dipole number is actually coupled to the variable r', concretely, dipole number is equal to the row of r'. The goal of this proposed global optimization method is to find the optimal location for dipole sets given dipole number. Equation (1) through (4) show the parameters that determines transfer matrix T.

$$T \sim r , r', f, \text{dipole type, orientation, number} \tag{35}$$

The overall optimization flow is shown below in Fig. 1.27.
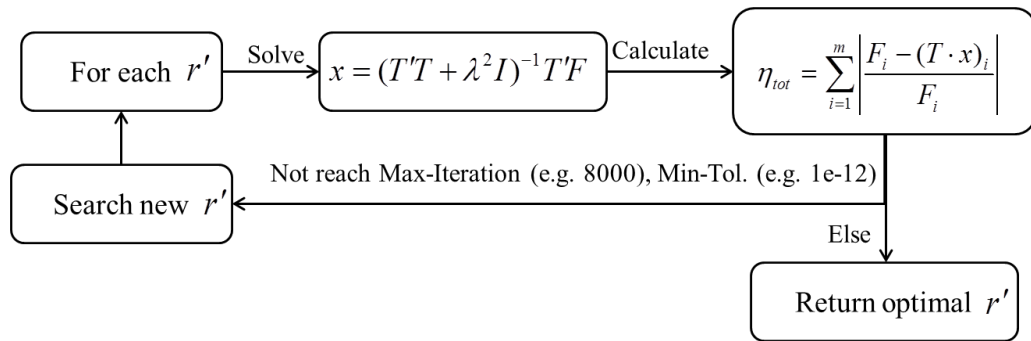
Figure 1.27. Optimization flow for searching optimal dipole sets distribution

Where η_{tot} is the total relative error summed up by each observation point, m is the total number of observation points. The algorithm takes a random initial location of dipole sets with given number to start. Then based on least square solution, the unknown magnitude and phase of dipole sets can solved. The objective function is calculated by summing up

the relative error of each observation points. If the convergence criteria is not met, then the algorithm continue searching for next r' and repeat the whole flow until it reaches the maximum number of iteration or the change of objective function is less than the tolerance. It is reasonable to set a constraint for r' that it is bounded by dimensions of radiator. Simulated annealing (SA) is used to solve this bound-constrained optimization problem. The method mimics the physical process of heating a material and then slowly cooling to decrease defects, thus minimizing the system energy [13]. Similar to but different from gradient descent algorithm, the SA algorithm tries to find a better solution at each iteration while it will also accept a solution that is worse than current solution with a certain probability. This can prevent the solution from trapping into local mimina/maxima.

In order to compare the performance of plain least square method and global optimization method, there are four groups of simulation data to verify it as shown in Fig. 1.28.
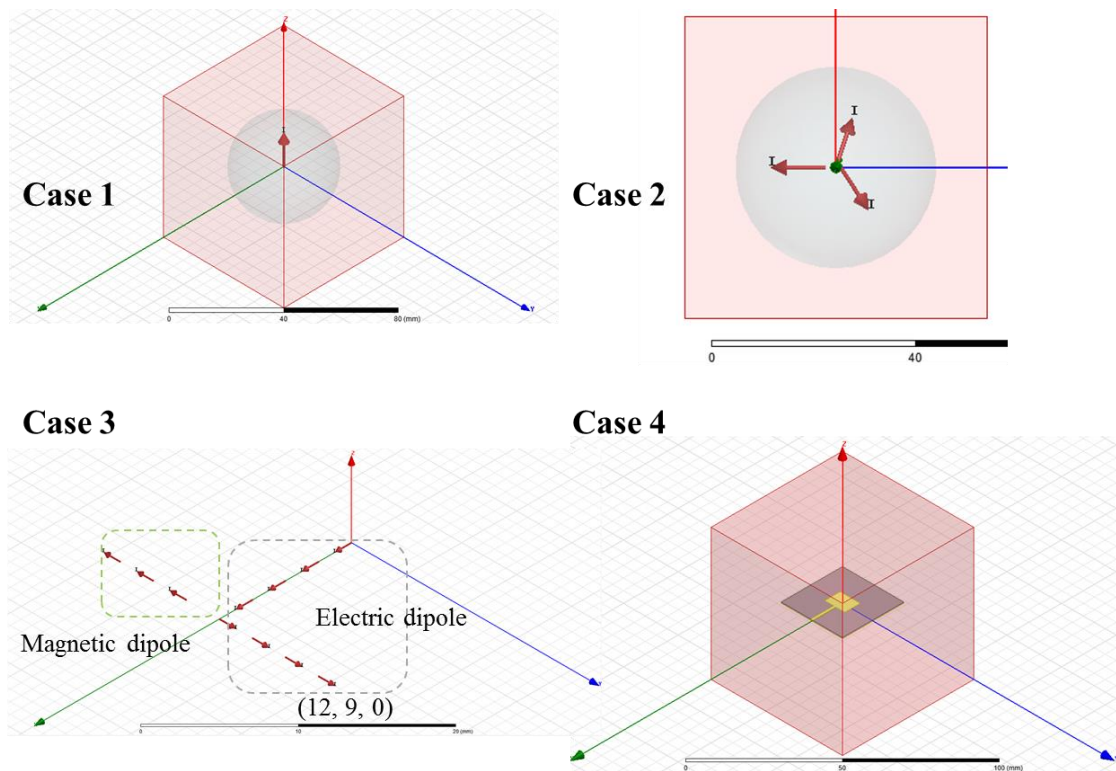
Figure 1.28. Simulation cases for validating dipole moment model extraction by global optimization method

In case 1, the radiation source is specified as an infinitesimal current segment locating at origin along z direction (Pz) with magnitude equals to 0.001 $A \cdot m$ and 0 phase. In case 2, there are three dipoles randomly locating at three different locations where one of them is magnetic dipole and the others are electric dipole, the magnitude of the dipole are also randomly set to 0.002 v/m, 0.001 $A \cdot m$ and 0.001 $A \cdot m$ to evaluate the performance of the proposed method. In case 3, there are two groups of dipoles, one of them is magnetic dipoles aligning along y direction, and the other is electric dipoles forming an L shape, the magnitude and phase are randomly chosen as in case 1 and 2. In case 4, the patch antenna is locating on a ground plane with dimensions 28mm by 28mm, the length of the patch antenna is 9.12 mm along y direction, and width is 7.02 mm along x direction. For four cases, the observation points are on a sphere with radius equals to 20 mm.

Since case 4 is a more general case, the following analysis will be based on case 4. At last, all four cases will be analyzed and compared in terms of error and stability. For the dipole model extraction method introduced above, the dipole sets are distributed uniformly on a plane. For global optimization method, the dipole sets are randomly distributed inside the bound of radiator. For case 4, the number of dipole sets is pre-defined as 20 at this stage, and the dipole sets distribution in least square method (LSQ) and in optimization method is shown as in Fig. 1.29. For LSQ method, the dipole sets is arranged as 2 by 10 arrays while for optimization method, the dipole sets are randomly distributed.

Dipole Distribution in LSQ   Initial Dipole Distribution in Optimization
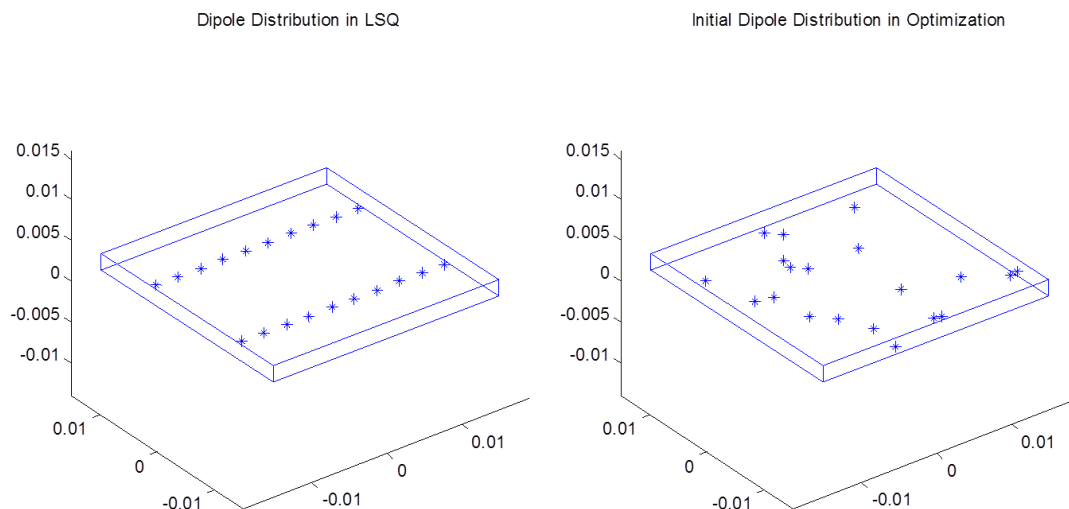
Figure 1.29. Initial dipole sets distribution for LSQ and optimization method

After running optimization, the dipole sets distribution will be optimized and shown in Fig. 1.30.

Dipole Distribution in LSQ   Optimal Dipole Distribution in Optimization
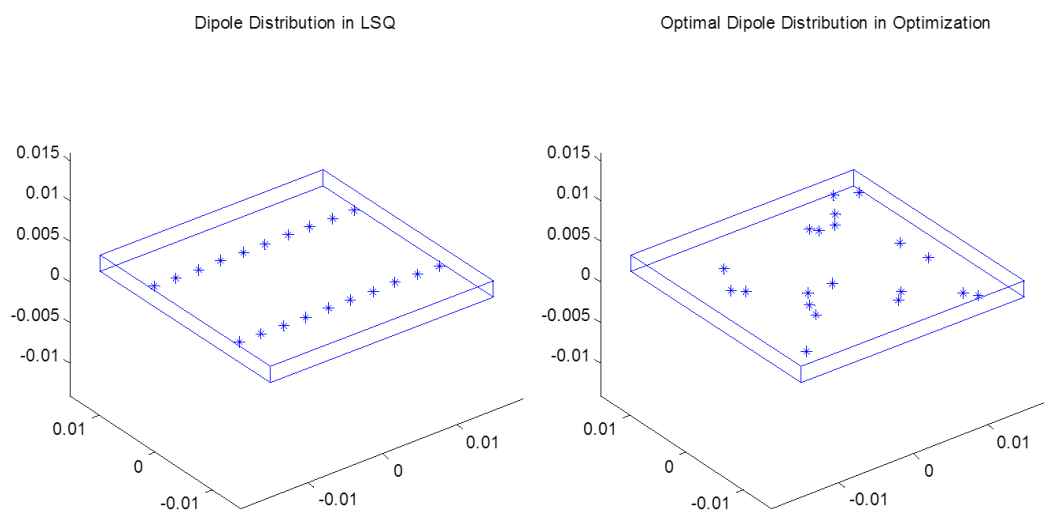
Figure 1.30. Optimal dipole sets distribution for LSQ and optimization method

The dipole moments can then be solved by LSQ and optimization respectively with the dipole distribution shown above. With equivalent dipole moment model, the field at sphere with radius equals to 25 mm is calculated by equation (18) and shown in Fig. 1.31 and Fig. 1.32. The total error is shown in Fig. 1.33.
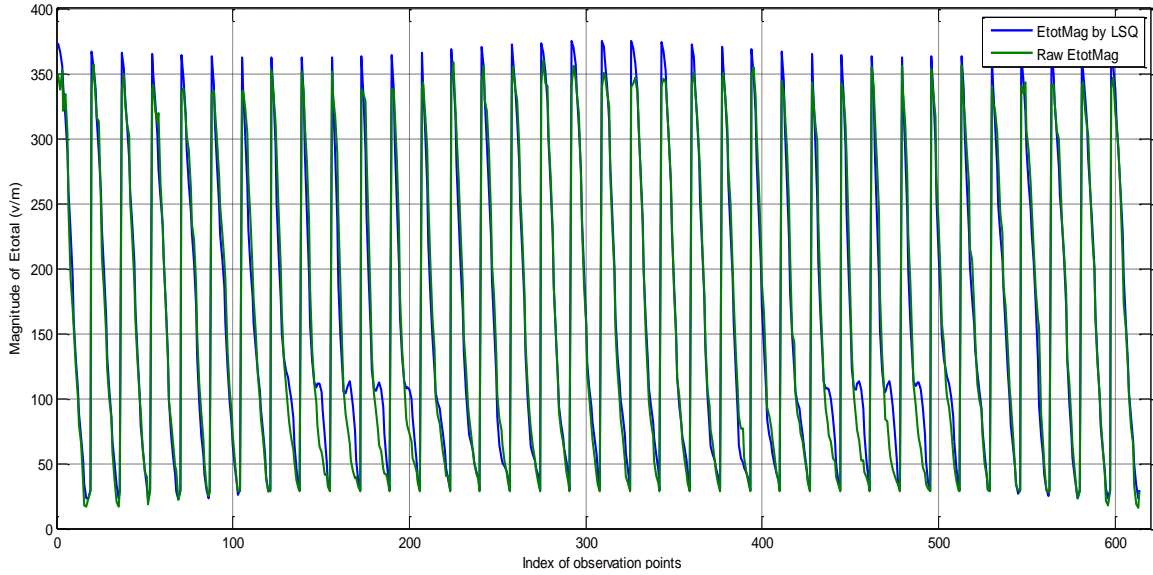
Figure 1.31. Total E field magnitude comparison between simulation and LSQ
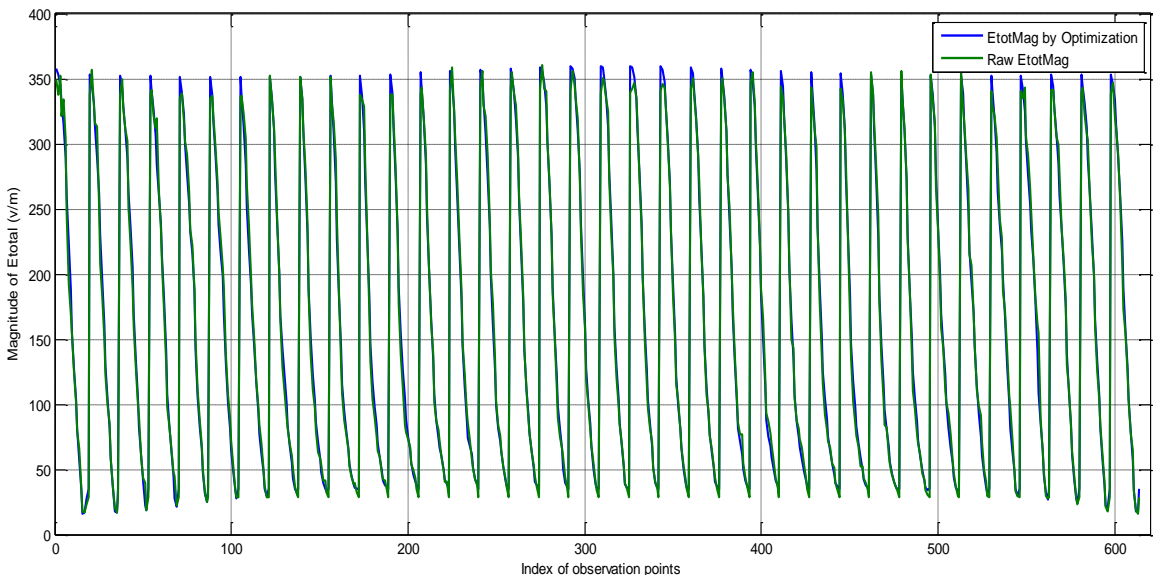
Figure 1.32. Total E field magnitude comparison between simulation and optimization

The horizontal axis denotes the index of observation point on sphere with radius equal to 25 mm. The vertical axis denotes the magnitude of observed total E field. It can be found that the discrepancies between raw data and fitted data using LSQ is relatively larger than the discrepancies between raw data and fitted data using optimization method.
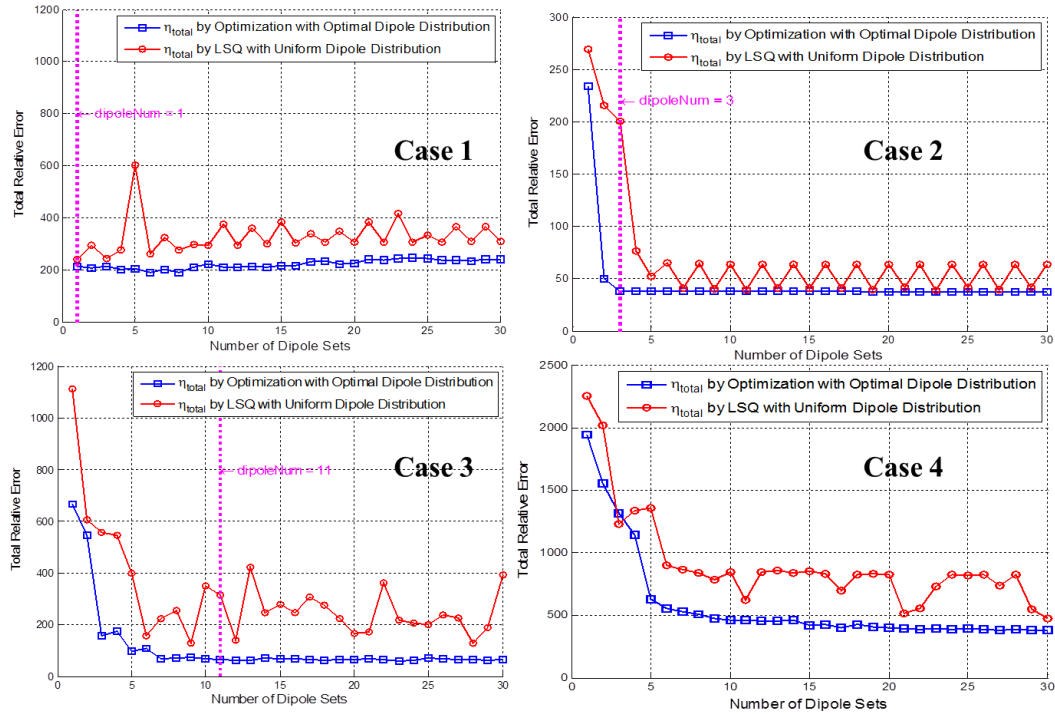
Figure 1.33. Total relative errors comparison between LSQ and optimization

Mathematically, the LSQ method will always give a solution with given dipole number and location. The global optimization method takes advantage of LSQ method and tries to search for a better dipole location at each iteration. Theoretically the total relative error of optimization method will not be greater than the total error of LSQ method. There may be a controversy that the LSQ method in the example above is put in a bad situation that the dipole array is not well arranged based on the nature of radiation pattern of patch antenna. To test the stability of both methods, all the four cases are studied and compared. With varying number of dipole sets, the total relative error of each case using both methods is shown in Fig. 1.33. In all the cases, the LSQ method arrange the dipole array as 2 by 10 while the optimization method arrange the dipole array in a random fashion as shown in Fig. 1.29.

For case 1, the true solution is one Pz dipole set. As the number of dipole increases, the total relative error first converges and later begins to increase. And the total error by optimization method is smaller than the total error by LSQ method for any dipole number. For case 2 and 3, the true solution is 3 and 11 dipole sets respectively. The LSQ method is oscillating after certain number of dipole sets while the optimization

method converges. For case 4, the optimization method is also better than LSQ method. It indicates how many dipole sets to choose after observing the convergence of total relative errors. Another dipole configuration scheme for LSQ method is shown in Fig. 1.34.
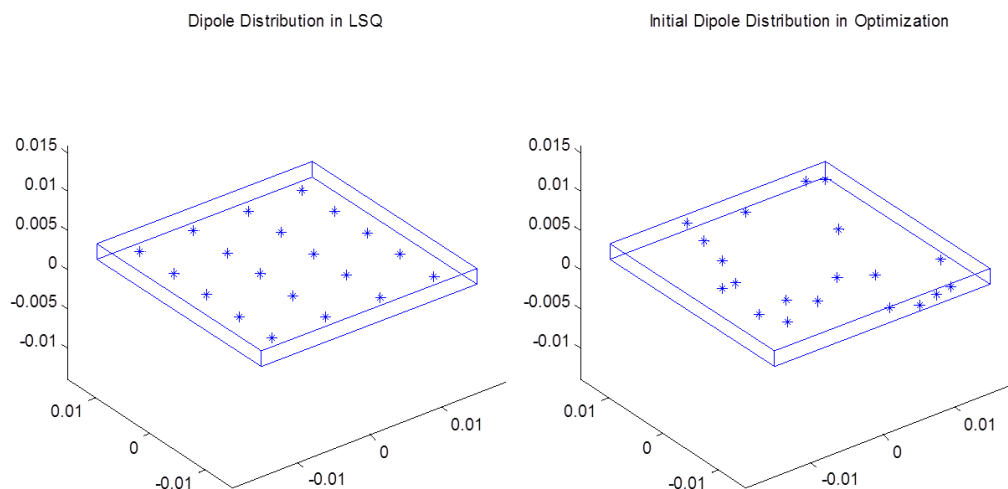
Figure 1.34. Initial dipole sets distribution for LSQ and optimization method

The motivation is show if the optimization method always has less error than LSQ method regardless of initial dipole distribution. In this case, the dipole distribution for LSQ is a 4 by 5 array that is to equivalently replace the patch antenna. The initial dipole distribution for optimization is still random. After SA optimization, the optimal dipole distribution is changed as shown in Fig. 1.35.
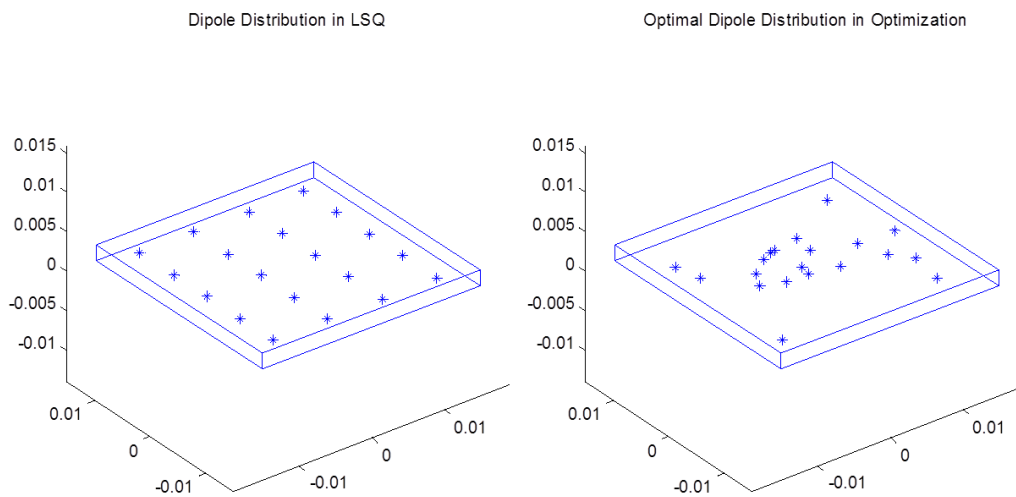
Figure 1.35. Optimal dipole sets distribution for LSQ and optimization method

For this dipole distribution scheme, the total relative error between LSQ and optimization is shown in Fig. 1.36.
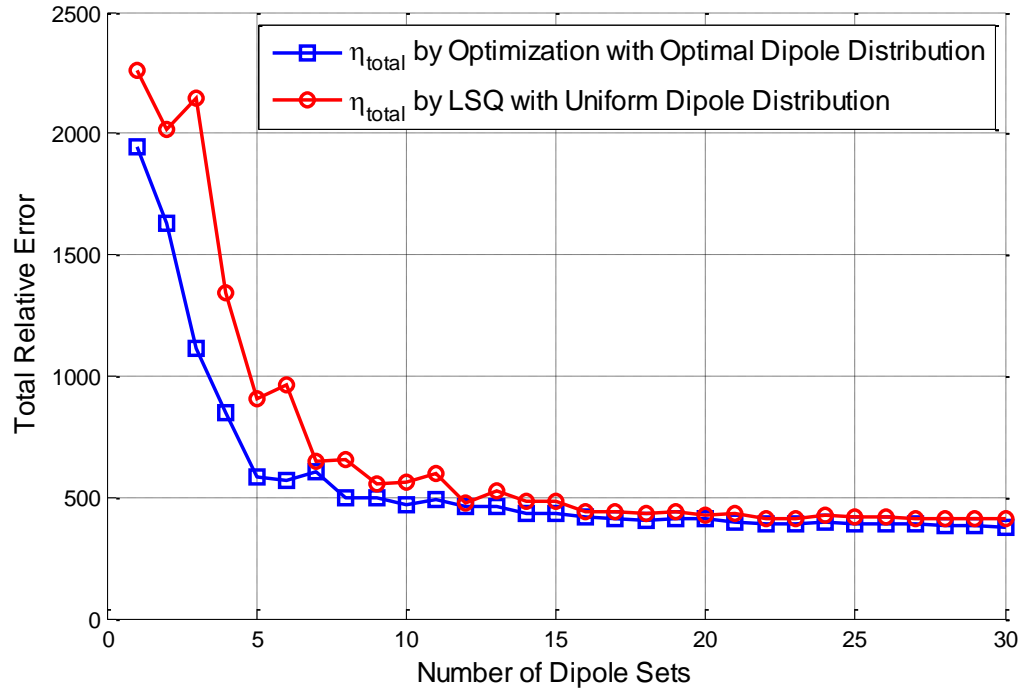
Figure 1.36. Total relative errors comparison between LSQ and optimization for case 4

The total error between LSQ method and optimization is smaller the previous case 4. The difference is that LSQ method uses different fixed dipole distribution scheme while the optimization uses random distribution and later optimize the distribution of dipole sets. In this case, the optimization method seems to have little advantage over LSQ method. From another perspective, the optimization method can always have stable performance and less total relative errors regardless of initial dipole distribution. To make LSQ equal performance, a good pre-defined dipole distribution is needed based on empirical rules. This is difficult when the radiator becomes complicated, such as a working camera module with modulated signal in the cellphone. In terms of calculation time, the LSQ method takes about 0.08s to solve the least square solution with dipole number equal to 20; while the SA optimization method takes about 403s to find the optimal dipole distribution with dipole number equal to 20 as shown in Table 2.1.

Table 2.1. Time consumption and accuracy

Algorithm	Max Iterations/ Generations	Tolerance	Dipole Sets Distribution	Time consumed (n = 20)	Average Error (%)
LSQ (Least-square)	1	N/A	Uniform (4×5)	0.08s	23.00
GA (Genetic Algorithm)	6000	1e-6	Random (20)	7894s	21.16
SA (Simulated Annealing)	8000	1e-12	Random (20)	403s	21.45

1.2. HUYGENS'S EQUIVALENT MODEL

In Huygens's equivalence principle, the actual sources are replaced by equivalent sources, and the equivalent sources produce the same fields as the actual sources within the region of interest [3]. Fig. 1.37 shows three cases for Huygens's equivalence principle. By the surface equivalence theorem, the field outside an imaginary Huygens's surface is obtained by putting equivalent surface electric and/or magnetic current over the surface. The actual radiating source is denoted as current densities J_1 and M_1. The radiated fields are denoted as E_1 and H_1 in homogenous medium (ε_1, μ_1). $\hat{n}$ is unit normal vector pointing outward. Equivalently, the radiating source can be replaced by surface electric and magnetic current (Love's equivalent Fig. 1.37(b)), or by surface magnetic current with PEC filled inside (PEC equivalent Fig. 1.37(c)), or by surface electric current with PMC filled inside (PMC equivalent Fig. 1.37(d)).
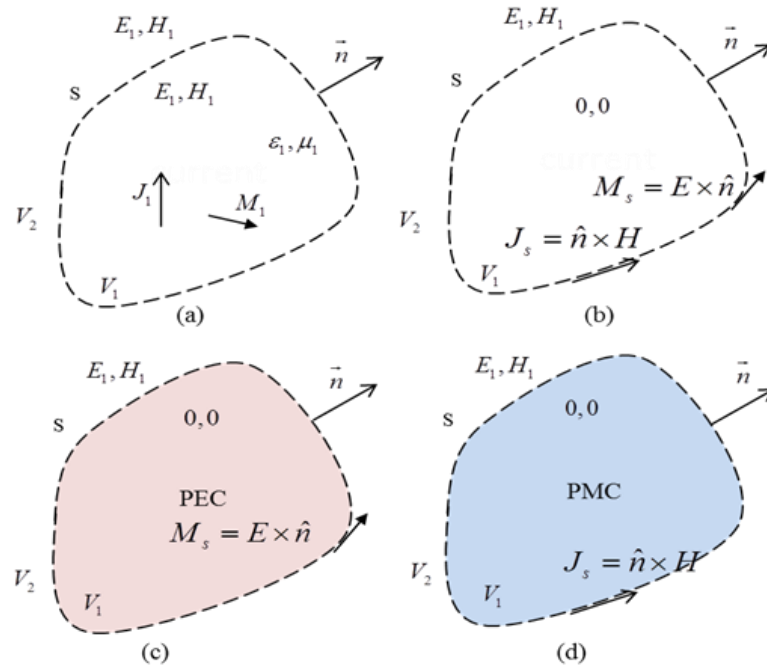
Figure 1.37. (a) Original source. (b) Love's equivalent. (c) PEC equivalent. (d) PMC equivalent

1.2.1. Simulation Validation for Huygens's Equivalent Model. The Huygens's surface is chosen to be a rectangular box that facilitates near-field measurement or even simulation. In this case, the Huygens's box enclosing the patch antenna is formed by z = 0 mm, z = 5 mm, x = ±25 mm, y = ±20 mm planes as shown in Fig. 1.38.
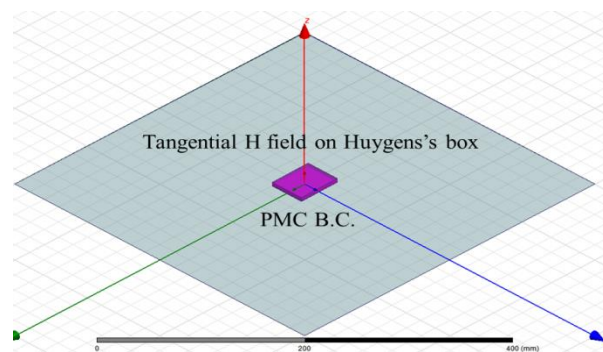
Figure 1.38. Equivalent Huygens's model for patch antenna in HFSS

Only tangential H field on the Huygens's box is used to calculate the equivalent surface electric current $J_s = \hat{n} \times H$. The inner volume of Huygens's box is filled with Perfect Magnetic Conductor (PMC) boundary condition according to the Huygens's principle. In

Fig. 1.38, the tangential H field on six surfaces is converted to the near-field source file format. The sampling spacing is 1 mm by 1 mm for all the surfaces. With tangential field data for each frequency point, all the files are then organized by a *.and file which is accepted for Huygens's equivalence simulation. More details about how to set up HFSS simulation with near-field source type can be found in [2]. The tangential E and H fields on z = 5 mm and z = 10 mm are shown in Fig. 1.39.
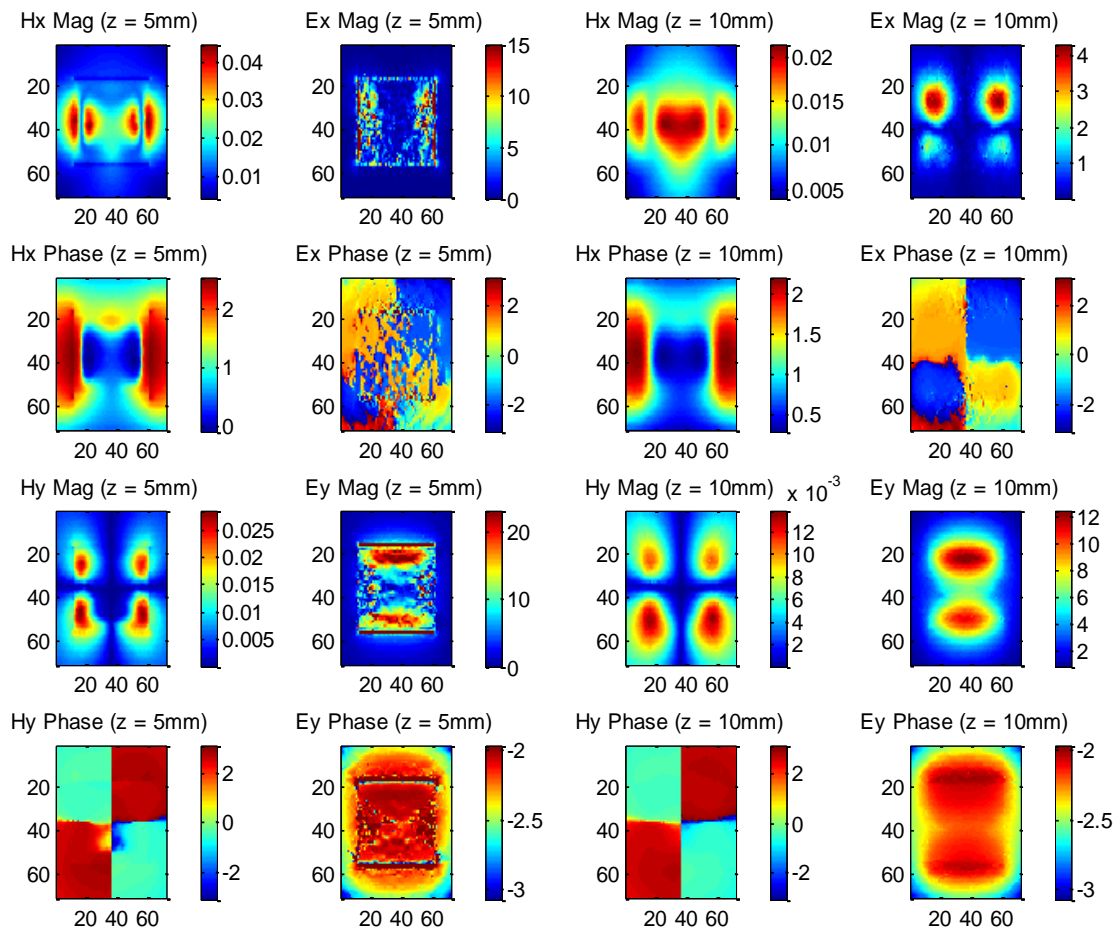
Figure 1.39. Tangential E and H field pattern at z = 5 mm and 10 mm from simulation of Huygens's equivalent model

The tangential fields can be reconstructed well at z = 10 mm, while there are some discrepancies at z = 5 mm in tangential E field. This could be caused by the finite size of mesh cells and finite convergence energy at the boundary. It can be seen that both dipole moment model and Huygens's equivalent model can model the original source. However, there are some differences between these two methods.

For dipole moment model, it has no unique solution to the linear equation mathematically (a.k.a. Inverse Problem). The solution accuracy is dependent on selection of dipole type, dipole number and dipole spacing etc. Currently there are not exact theoretical criteria to choose dipole number, dipole spacing etc. Empirical rules are used and the result turns to be acceptable based on some test cases as shown in [2][3].The optimization method of dipole model extraction is studied in [14][15] which finds the optimal dipole sets configuration, however, it consumes a lot of computation time. The advantage of using dipole moment model is that it can represent original source very well regardless of ambient scatters. For example, the dipole moment model of an IC without heat-sink can be used in the situations that same IC with heat-sink as studied in [6]. Another advantage of dipole moment model is that only tangential field on a plane is needed instead of a closed surface.

For Huygens's equivalent model, the model is determined by the total field on the Huygens's surface. Hence any nearby scatters that can change the field distribution will result in different Huygens's model. For example, if coupling from IC with heat-sink to victim antenna is desired, then the Huygens's model should be extracted when the heat-sink is present. In real measurement situation, this brings near-field scanning difficulty. Assume the Huygens's model is extracted when there is no heat-sink on top IC, the model is not suitable to estimate the coupling since the total field will be changed after putting heat-sink back. The advantage of Huygens's equivalent model is that it has unique noise source model based on uniqueness theorem.

1.2.2. Huygens's Model in Near-field to Far-field Transformation.

For governmental EMC requirements for electronic systems, standardized test and certification are mandatory before the products coming into the market. One significant contributor to the radiation in the electronic device is the IC as shown in Fig. 1.40. Measuring the far-field radiation from IC itself becomes meaningful since the radiation can be quantified and furthermore take action to suppress the radiation source.
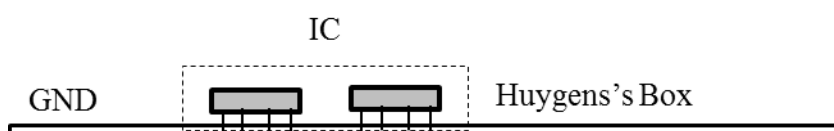
Figure 1.40. Equivalent Huygens's model for IC radiation

The near-field scanning technique makes it possible to acquire the total field information from the IC in the near-field as shown in Fig. 1.40. There are several methods for near-field to far field transformation, Huygens's equivalence principle, plane/spherical wave expansion etc. The method used here is the Huygens's equivalence principle as shown in Fig. 1.41 since commercial software can be leveraged to solve the problem conveniently and fast. The noise source in this part is a clock module with several working IC. The main objective is to estimate the far-field zone E field strength of IC by the IC near-field scanning measurement.
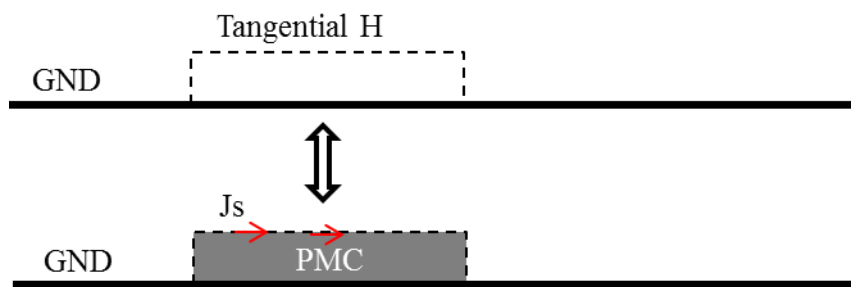
Figure 1.41. Extracting equivalent Huygens's model

In near-field scanning measurement, only H-probe is used to get tangential H field as shown in Fig. 1.41. With Huygens's principle, the surface equivalent electric and magnetic currents are obtained and apply FEM to calculate the E field in the far-field zone. Once get the near-field data from measurement, format the data and import them into commercial simulation tool HFSS or CST [16] to get the far-field radiation. In the thesis, only simulation in HFSS is introduced.

In the near field scanning, only H probe is used to get H field and then apply Huygens's principle to calculate the equivalent surface electric current and then calculate the radiation at far field zone. The overall flow of near-field to far-field transformation is shown in Fig. 1.42.
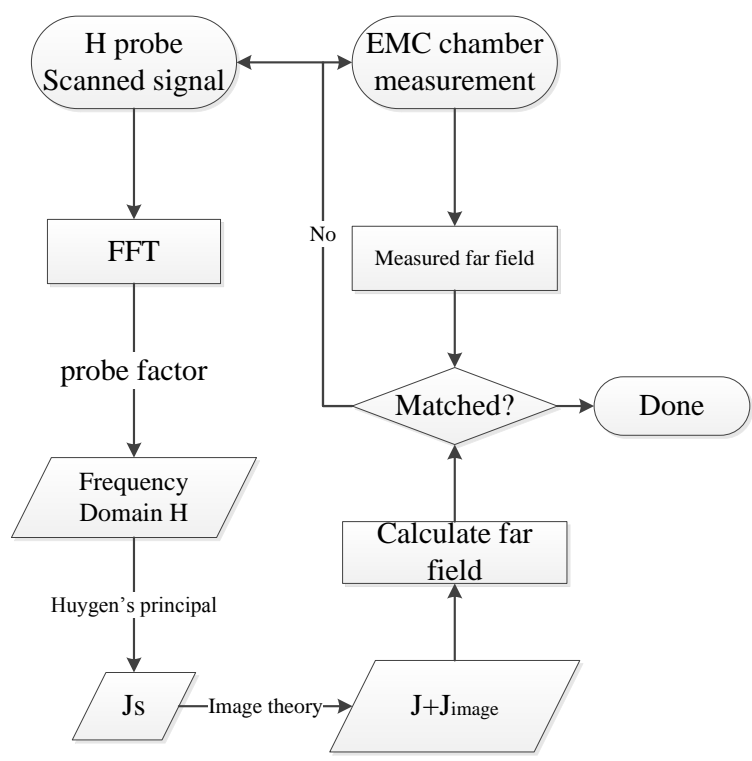
Figure 1.42. Overall flow of Near-field to Far-field transformation by equivalent Huygens's model

In near-field scanning, both magnitude and phase information are needed, hence a phase measurement method by synchronizing with the source is proposed. Afterwards, the measured voltage will be converted to H field by multiplying the probe factor. Huygens's principle requires a closed surface or infinitely large plane; here a five surface Huygens's box is used in measurement as shown in Fig. 1.43. Only tangential field are measured.
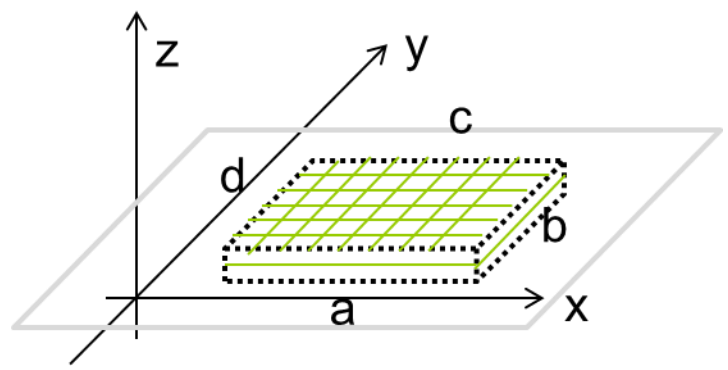
Figure 1.43. Huygens's surface in real measurement

For top surface: the tangential components are Hx and Hy. For side surface: along x direction, the tangential component are Hx and Hz, while base on boundary condition: the normal H field vanishes at the PEC boundary. Although the scanned H field are not right at the PEC boundary, the Hz component is approximately equal to zero as the scanning height is small and $\frac{\partial Hz}{\partial n}$ is also small which means the Hz component doesn't change much from zero. Similarly, along y direction, the tangential component can be Hy only.

For the test board shown in Fig. 1.44, the working IC array is exposed and all other parts are shielded with copper tape. In measurement, the phase is measured by a scope. There two channels, one is the reference signal and the other is the probe signal as shown in Fig. 1.45.
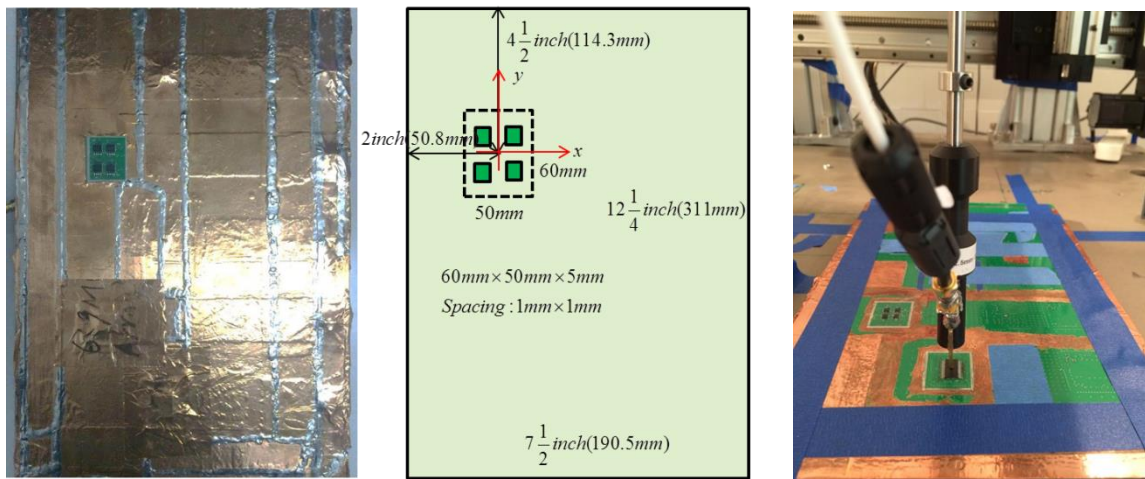
Figure 1.44. Test board dimensions and near-field scanning
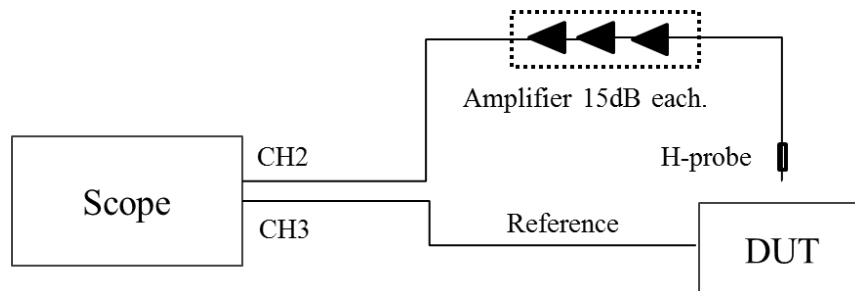
Figure 1.45. Diagram of overall setup

At each scanning point, the scope stores the voltage waveform and continues to next point. With all the scanning points' data, FFT is applied to get the frequency data. Then multiple the frequency data by the probe factor, the measured H field is acquired. The scope is triggered on reference signal with averaging. The sampling frequency is 4 to 5 times as the highest harmonic frequency, this will acquire sufficient frequency information. The memory depth relies on the IC working frequency and the sampling rate. In order to capture N clock cycles of the IC, the corresponding memory depth can be calculated as

$$\text{Mem. Depth} = \frac{\text{Sampling Rate}}{\text{IC working frequency}} \times N \tag{36}$$

There are two measured IC array data available. The tangential H field magnitude pattern radiated by 125 MHz IC array is shown in Fig. 1.46.
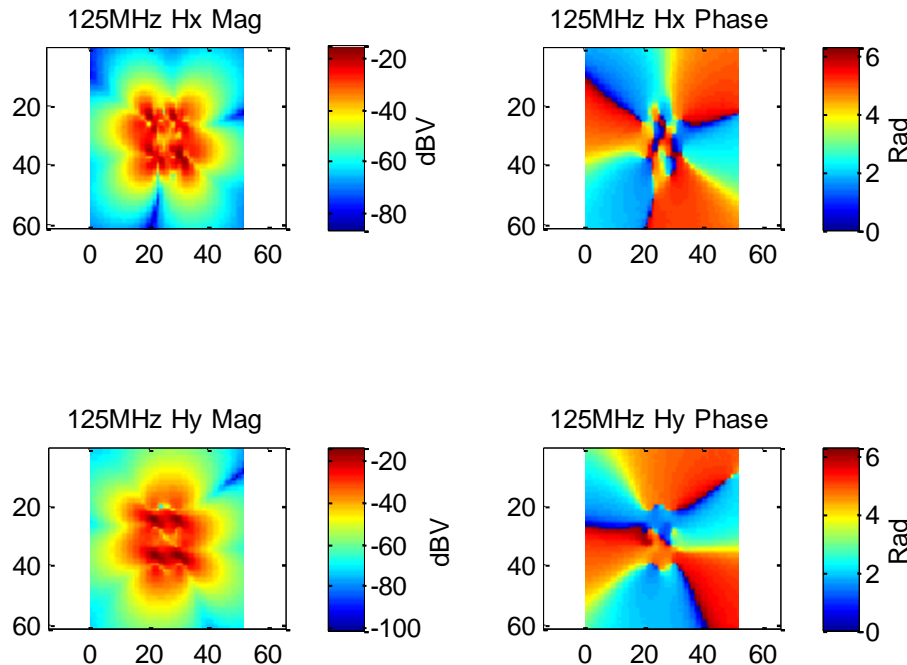
Figure 1.46. Tangential H field pattern at 125 MHz by near-field scanning

The tangential H field of 669 MHz IC array from near-field scanning is shown in Fig. 1.47. With tangential H field obtained from near-field scanning, the equivalent dipole moment model can be extracted based on the discussion above in Section 1.1. Theoretically, the field at anywhere can be calculated based on superposition of each

individual dipole's radiation. In this Near-field to Far-field transformation application, the field at far-field is estimated based on the dipole moment model.
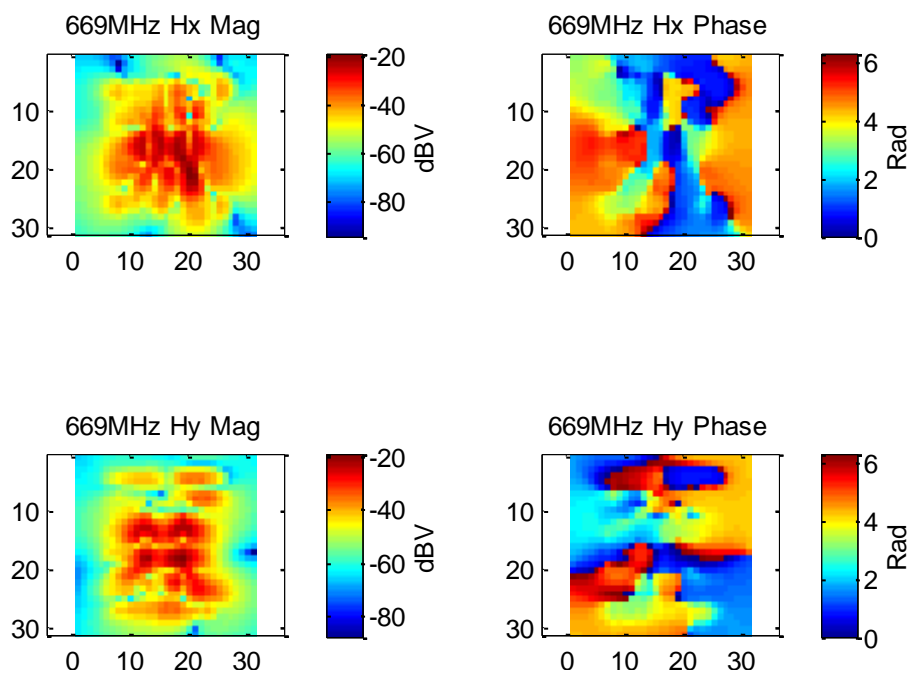
Figure 1.47. Tangential H field pattern at 669 MHz by near-field scanning

The maximum Ez magnitude is also obtained by measuring in the EMC chamber as shown in Fig. 1.48. The overall setup is shown below.
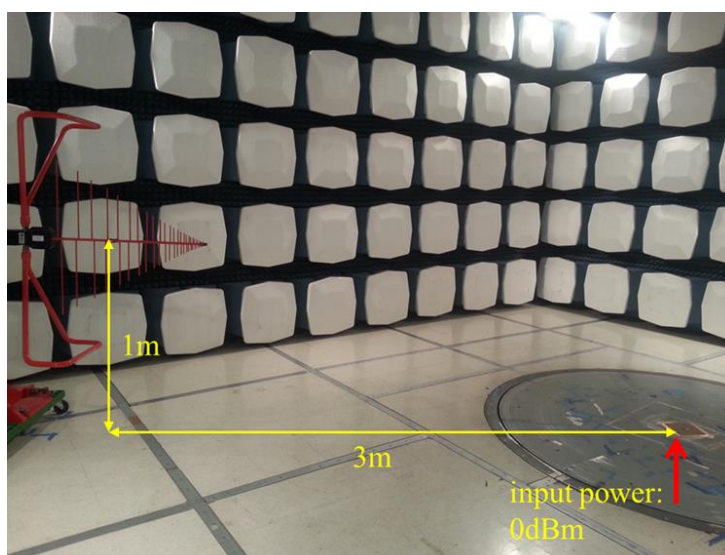
Figure 1.48. Far-field measurement in EMC chamber

The E field is converted by equation (37)

$$E(dBuV/m) = Power + AF + 107 \qquad (37)$$

The comparison between estimated maximum Ez with equivalent dipole moment model and measured Ez in EMC chamber for 669 MHz IC array is shown in Fig. 1.49.
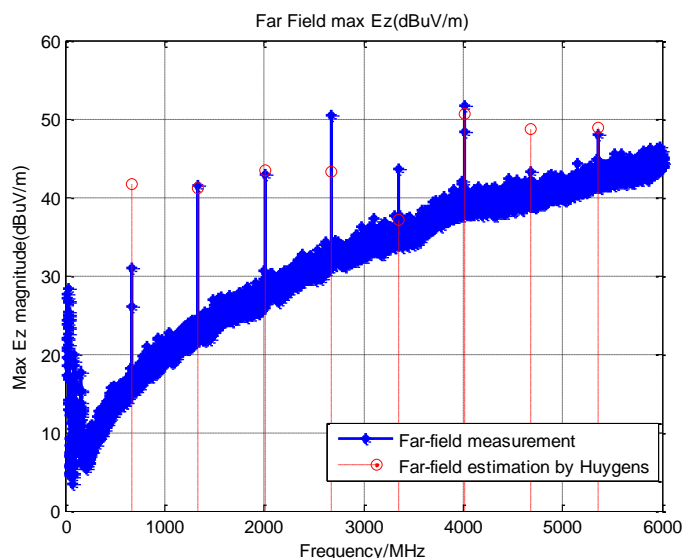
Figure 1.49. Far-field comparison between measurement and Huygen's model prediction

The comparison between estimated maximum Ez with equivalent dipole moment model and measured Ez in EMC chamber for 125 MHz IC array is shown in Fig. 1.50.
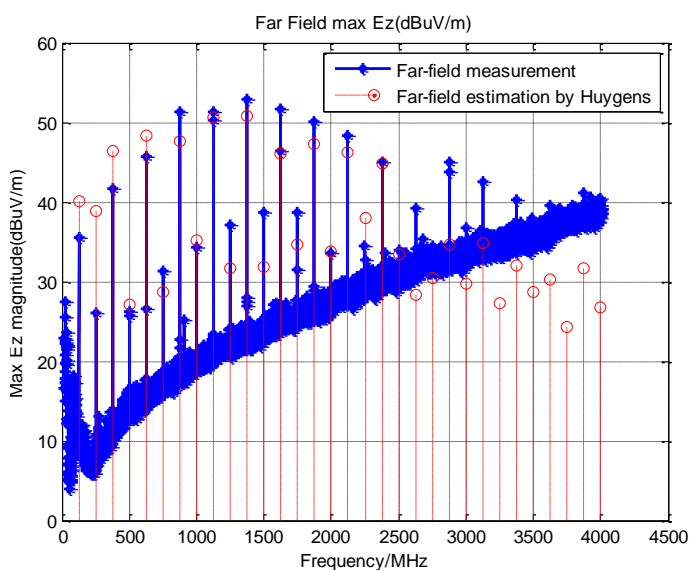
Figure 1.50. Far-field measurement in EMC chamber

In general, the difference between the measurement and the Huygens's estimation is small. For most frequency harmonics, they are less than 5 dB. This is meaningful for engineering application. The result accuracy depends on both the probe factor and near field measurement accuracy. Besides, the simulation setup like GND dimension and mesh could also affect the result. Phase measurement can also be done with VNA to further improve the measurement precision since it has better sensitivity and signal to noise ratio. It should be clear that, the field on Huygens's box is considered only comes from the IC source. This is not practical in the real scanning environment. The scattering issue arises when there is a scatter near the DUT.

1.3. SUMMARY AND FUTURE WORK

The radiation noise source can be modeled by dipole moments or Huygens's model. For least-square method, the limitation exists in the selection of dipole sets, which is improved by optimization method. The optimization method has better overall performance than LSQ method. In dipole moment method, the conducting plane is assumed to be with finite size. The diffraction caused by edge effects can be more dominant as the size of ground plane is becoming smaller. For Huygens's model, the total tangential field determines the model which implies the model may be different if the total field is different. In this case, the multiple scattering effects play a critical role in modeling. To avoid solving inverse problem, the dipole type, orientation, number and location should be all optimized. This needs further investigation to compare the performance of optimization and LSQ method.

2. NEAR-FIELD COUPLING ESTIMATION IN RF INTERFERENCE

2.1. DIRECT METHOD

Radiation noise source modeling is the key to estimating the near-field coupling in RF interference analysis. With equivalent radiation model of the source, the coupling between radiation source and victim antennas can be predicted directly by simulation or analytical calculation.

In Section 1, two methods of noise source modeling are presented. One is equivalent dipole moment model and the other is Huygens's equivalent model. With equivalent noise source model, the near-field coupling between radiation noise source and victim antennas can be estimated. The coupled noise power originates from the noise source is calculated by integrating over the entire victim antenna port of the real part of the normal Poynting vector. The Huygens's equivalent source to victim antenna coupling calculation is implemented in full-wave simulation tool while the equivalent dipole moment model can be either imported in simulation tool or applied in analytical calculation. Applying dipole moment model to near-field coupling is studied in [17]. Only Huygens's model method is discussed in the following sections.

2.1.1. Simulation Validation. A simple model is created for verifying the Huygens's equivalence principle method for near-field coupling in HFSS. In Fig. 2.1, a vertical Hertzian dipole is used to represent a small radiating current segment. And a patch antenna working at 2.4 GHz is located nearby.
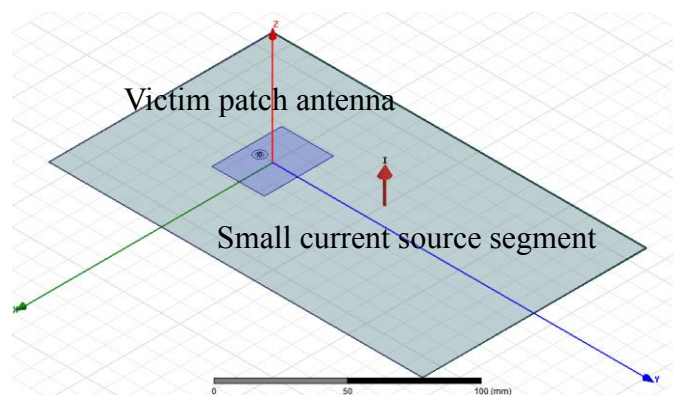
Figure 2.1. A small current source segment to patch antenna coupling model

The patch antenna dimension is 37.2 mm by 28 mm by 0.036 mm. The distance between current source and victim patch antenna is 60 mm along y axis, and the height of the current source is 10 mm above the ground. Another Huygens's equivalent model is shown in Fig. 2.2. The Huygens's box is 40 mm by 40 mm by 40 mm. The excitation is distributed over the entire Huygens's box as the equivalent surface electric current source. And the equivalent source is obtained by the tangential H field from Fig. 2.1 by

$$J_s = \hat{n} \times H \tag{38}$$

Figure 2.2. Equivalent Huygens's model representing actual current source segment

In Fig. 2.2, the tangential H field on six surfaces is converted to the near-field source file format. The sampling spacing is 1mm by 1mm for all the surfaces. With tangential field data for each frequency point, all the files are then organized by a *.and file which is accepted for Huygens's equivalence simulation. The near-field source file format is described with an example in Table 2.2. The table records the complex H field at (x, y, z) for specified frequency point.

Table 2.2. *.nfd file specification

#Index	X	Y	Z	Hx		Hy		Hz	
				Re	Im	Re	Im	Re	Im
Frequencies				1					
Frequency				f(2.0e9-3.0e9)					
1	…	…	…	…	…	…	…	…	…

Then the Huygens's box information and equivalent source type is specified in the *.and file as describe in Fig. 2.3. The 'NearFieldHeader' part describes the simulation parameters and the 'NearFieldData' specify the near-field data [7].

```
$begin 'NearFieldHeader'
        type = 'nfd'
        fcoords = 'cartesian'
        fields = 'H'
        geometry = 'box'
        center = '0mm, 60mm, 20.356mm'
        size = '40mm, 40mm, 40mm'
        fsweep = '2.000000GHz, ..., 3.000000GHz'
$end 'NearFieldHeader'

$begin 'NearFieldData'
        FreqData("2.000000GHz", "Dipole40by40by40_2G_3G_2000MHz.nfd")

        ...
        FreqData("3.000000GHz", "Dipole40by40by40_2G_3G_3000MHz.nfd")
$end 'NearFieldData'
```

Figure 2.3. File description for equivalent source simulation

For the coupling at the victim antenna port, the coupled power from the source to the victim antenna is calculated by integrating the time average Poynting vector over the entire victim antenna port s. The coupled power comparison result is shown in Fig. 2.4.

$$P_{av} = \int_s \text{Re}\{\vec{S}\} \cdot d\vec{s} = \frac{1}{2}\int_s \text{Re}\{\vec{E} \times \vec{H}^*\} \cdot d\vec{s} \tag{39}$$

In the working frequency band, the coupled power by actual source and Huygens's equivalent source has difference less than 5 dB which is acceptable for engineering purpose. And the deviation at frequencies close to 2 GHz and 3 GHz can be caused either by the mesh cell size or the received radiation strength from the source. The simulation verifies that the Huygens's model can be used to equivalently replace the original model.

Figure 2.4. Coupled power by actual source and equivalent source

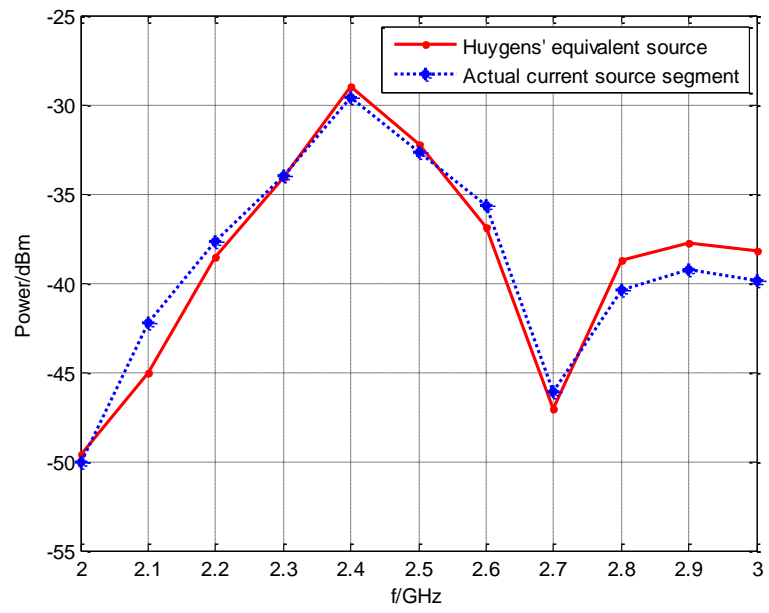**2.1.2. Measurement Validation.** A test board with IC and patch antenna is further used to validate the dipole moment model and Huygens's equivalence principle method. The test IC is a 2:8 clock buffer CDCLVP1208 with differential input and eight LVPECL output as shown in Fig. 2.5.
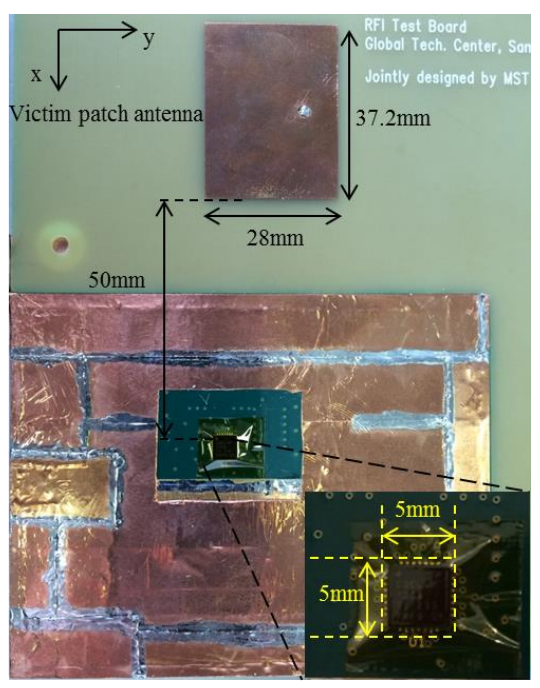

Figure 2.5. Test board with a clock buffer IC and victim patch antenna

First the IC is scanned with H field probe, the H field probe is calibrated to get the probe factor which includes the magnitude and phase information of the probe and connecting cables and amplifiers. H field probe is 5 mm above the GND plane with working frequency up to 9 GHz. This phase-resolved probe calibration and measurement in near-field scanning is similar to that in [18][19][20]. The scanning diagram and setup for the test board is shown in Fig. 2.6.
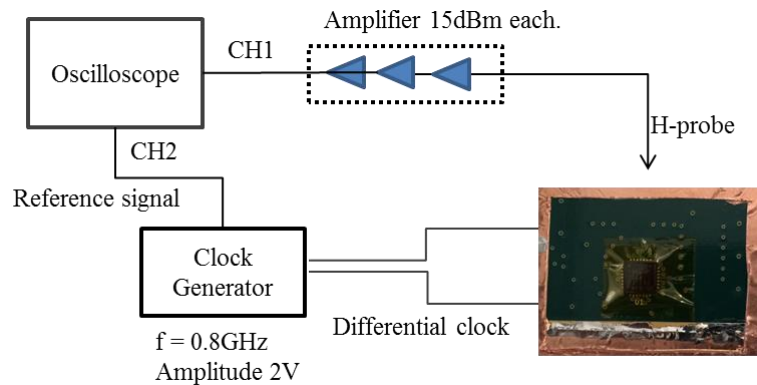
Figure 2.6. Diagram of IC near-field coupling measurement

In real measurement setup, the clock generator is the PRBS generator which has differential clock output and extra clock output. The reference signal comes from the extra clock output whose frequency is ¼ of the differential clock. The reference signal frequency is not necessarily ¼ of the driving frequency, as long as it is synchronized with driving frequency. The oscilloscope is triggered on the reference signal to synchronize the probe signal and the reference signal. The PRBS generator is put outside the chamber since the instrument radiation can also be picked up by the victim antenna. Besides, the cable connecting the PRBS generator and IC is surrounded by two current clamps to suppress the common mode current for individual cable and the cable- chamber ground system. The measured H field pattern selected at 2400 MHz is shown in Fig. 2.7. The magnitude and phase have smooth variation and locates at the center of the scanning plane. This indicates the field result is physically reasonable. Consequently, the dipole moment model is extracted based on the near-field scanning data. The dipole moment model is an array with 21 by 21 along x and y direction. The spacing of each dipole is 3 mm, and the dipole array height is 1.5 mm from the ground plane.
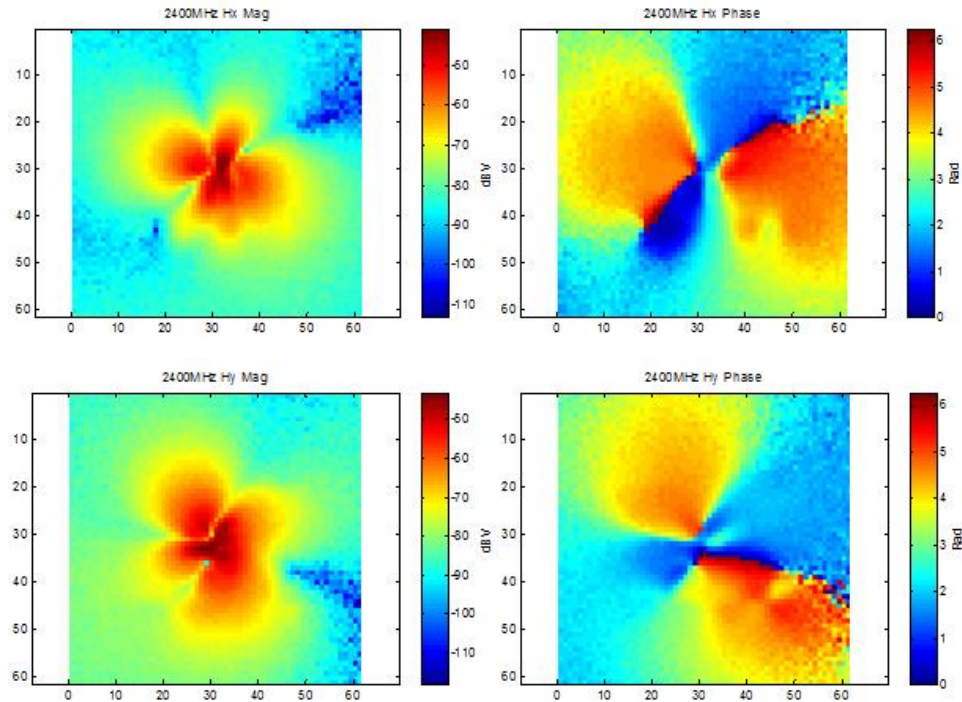
Figure 2.7. Measured Hx and Hy magnitude and phase at 2.4 GHz

Basically the dipole spacing is determined by the field pattern rather than the geometry of the IC, i.e. with more rapid changing field pattern, the dipole spacing becomes smaller in order to obtain higher spatial resolution. The dipole array center is the same as the scanning plane center which has the maximum radiation based on Fig.2.7. The simulation model is shown in Fig. 2.8.
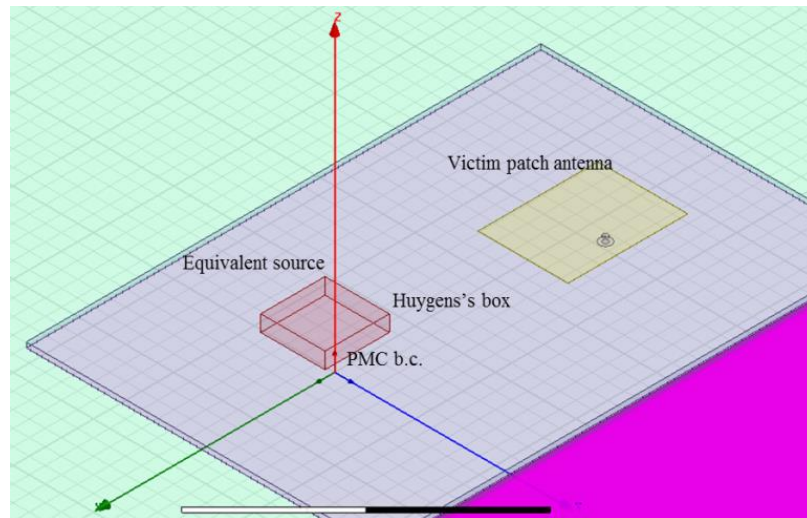
Figure 2.8. IC replaced by equivalent Huygens's source

With the dipole moment model, the tangential H field on an imaginary Huygens's box can be calculated by equation (18) with normalization. Convert the calculated tangential H field data to the specified data format introduced in section IV. The test board is modelled in full-wave simulation tool. The model is shown in Fig. 2.8.

For simulation, the coupled power is calculated by equation (39). The direct IC to patch antenna coupled power is measured by spectrum analyzer with diagram shown in Fig. 2.9. The measured power from Fig. 2.9 and power calculated from Huygens's equivalent source is compared in Table 2.3.
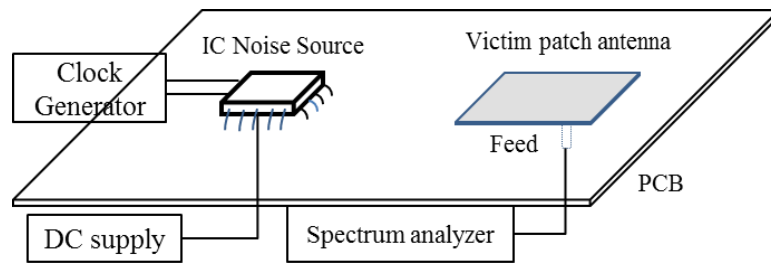
Figure 2.9. Direct coupled power measurement diagram

Table 2.3. Coupling from IC to antenna comparison

f(GHz)	0.8	1.6	2.4	3.2	4.0	4.8	5.6
Measured (dBm)	-111.5	-103.0	-93.5	-107.5	-96.5	-98.0	-104.5
Simulation (dBm)	-108.7	-101.3	-95.3	-103.3	-104.0	-105.2	-105.4
Difference (dB)	-2.8	-1.7	1.8	-4.2	7.5	7.2	0.9

The measurement power and simulated power is less than 8dB from fundamental frequency to the 7th harmonic of the IC driving clock. Near the working frequency of the victim antenna, the coupling has good estimation with less than 3 dB difference. Since the victim antenna locates in the near-field zone of the radiating source which has rapid changing electromagnetic fields, the error may come from either the spatial sampling distance in near-field measurement or the finite mesh size setup in simulation. This is critical as the frequency goes higher the electrical distance between source and victim antenna is relatively larger.

2.2. RECIPROCITY METHOD

A reciprocity theorem based decomposition method is introduced in [21] for near-field RFI analysis. Basically, the overall problem can be divided into two parts. The first part which is defined as forward problem is to characterize the radiation source and obtain the tangential field on Huygens's surface. The second part which is defined as reverse problem is to find out what the resultant E and H field on the Huygens's surface are due to known excitation. Finally, the coupled voltage from source to victim is estimated by reciprocity theorem with tangential field obtained in both forward problem and reverse problem.

The main goal of this section is to validate the reciprocity theorem method proposed in [21] to an active IC source by measurement. The detailed implementation for a passive structure is studied in [19]. The reciprocity method is first reviewed and then the corresponding implementation of measurement is introduced. In general, the noise source is modelled as equivalent dipole moments by solving the linear least square problem with fields obtained from near-field scanning plane [1]. The victim antenna is modelled in full-wave simulation tool since its structure is relatively easy to model, and the Huygens's surface is enclosing the victim antenna due to compact geometry of the victim antenna. Finally, the coupled voltage at the antenna port can be calculated by numerical expression of reciprocity theorem.

2.2.1. Reciprocity Theorem. A simplified typical RF interference scenario is shown in Fig. 2.10. The noise source is specified as a working IC located on a large GND plane which conforms to most engineering application cases. And a patch antenna is located close to the IC noise source. The final objective is to find out what the coupled power is from the IC noise source to the neighboring patch antenna.
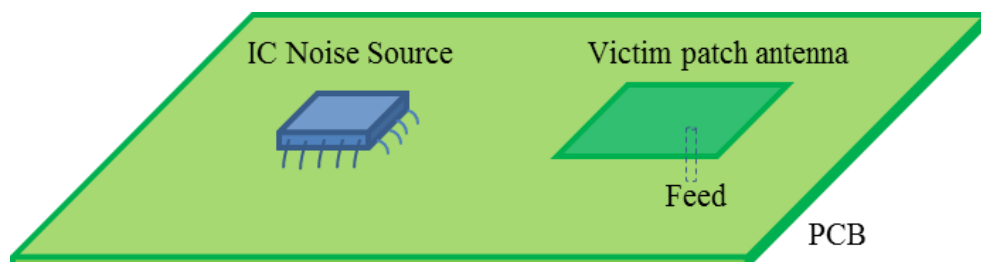

Figure 2.10. IC Noise source and nearby victim patch antenna

The basic idea for resolving this problem is by applying the reciprocity theorem to obtain the coupled voltage at the victim antenna port. The main efforts are spent on how to characterize the source and victim. Recall the reciprocity theorem for a reciprocal network in circuits, the ratio of response voltage to the exciting current remains the same after exchanging their locations as shown in Fig. 2.11. Where current is the excitation and voltage is the response.

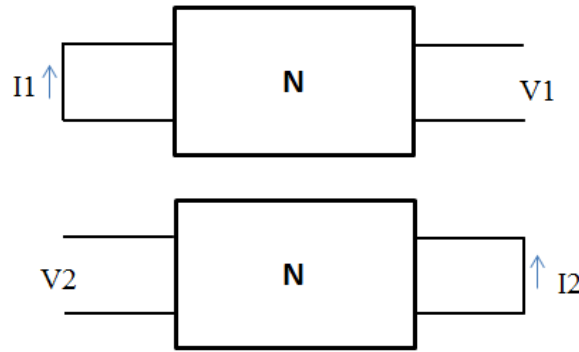$$I_1/V_1 = I_2/V_2 \tag{40}$$

Figure 2.11. Reciprocity theorem for a reciprocal circuit network

In analogy to the reciprocity theorem for circuit case, the reaction theory states that the reaction of the fields $(\vec{E}_1,\vec{H}_1)$ produced by source one $(\vec{J}_1,\vec{M}_1)$ to source two $(\vec{J}_2,\vec{M}_2)$ is equal to the reaction of the fields $(\vec{E}_2,\vec{H}_2)$ produced by source two $(\vec{J}_2,\vec{M}_2)$ to source one $(\vec{J}_1,\vec{M}_1)$ [22]. This can be expressed in the equation (41), where $<(\vec{J}_1,\vec{M}_1),(\vec{E}_2,\vec{H}_2)>$ denotes the reaction of fields two to source one.

$$<(\vec{J}_1,\vec{M}_1),(\vec{E}_2,\vec{H}_2)>=<(\vec{J}_2,\vec{M}_2),(\vec{E}_1,\vec{H}_1)> \tag{41}$$

Theoretically, if source one $(\vec{J}_1,\vec{M}_1)$, source two $(\vec{J}_2,\vec{M}_2)$ and field $(\vec{E}_2,\vec{H}_2)$ are known, the fields $(\vec{E}_1,\vec{H}_1)$ originate from source one can be derived. In terms of the problem discussed in this section, the working IC is denoted as source one and victim patch antenna as source two. The first step is to characterize the working IC, i.e. obtain the distribution of source one $(\vec{J}_1,\vec{M}_1)$. However, obtaining the current distribution of a working IC is very difficult if not impossible. Alternatively, the Huygens's surface equivalent currents $(\vec{J}_s,\vec{M}_s)$ are used to equivalently represent the IC source. The second

step is to get the response $(\vec{E}_2, \vec{H}_2)$ of a given excitation $(\vec{J}_2, \vec{M}_2)$. This can be done more easily since the patch antenna is a passive structure. The overall model is shown below in Fig. 2.12.

Figure 2.12. Simplified problem model

Based on equation (41) and the discussion above, the whole problem can be decomposed into two parts: the first part is defined as forward problem. In forward problem, the IC is powered on and the victim patch antenna is not excited. The second part is defined as reverse problem. In reverse problem, the victim antenna is excited and the IC is powered off. In summary, with tangential E and H fields on Huygens's box obtained in both forward and reverse problem, the coupled noise voltage can be estimated by reciprocity theorem whose detailed derivation will be shown in section five.

2.2.2. Numerical Derivation. As stated in [22], the integral form of Lorentz reciprocity theorem can be expressed using the field and source quantities in forward and reverse problem as explained in [21].

$$-\oiint_S (\vec{E}^{rev} \times \vec{H}^{fwd} - \vec{E}^{fwd} \times \vec{H}^{rev}) \cdot ds' = \iiint_V (\vec{E}^{rev} \cdot \vec{J}^{fwd} + \vec{H}^{fwd} \cdot \vec{M}^{rev} - \vec{E}^{fwd} \cdot \vec{J}^{rev} - \vec{H}^{rev} \cdot \vec{M}^{fwd}) dv' \quad (42)$$

Where S is the boundary surface of volume V, E^{fwd}, H^{fwd} represent the field radiated by source J^{fwd}, M^{fwd} in forward problem. Similarly, E^{rev}, H^{rev} represent the field radiated by source J^{rev}, M^{rev} in reverse problem.

Since the boundary surface S can be arbitrary shape as long as it encloses the source medium, one useful transformation of equation (41) can be evaluated by extending S to infinity. The field observed at infinitely far away is equal to zero. Thus the left side of equation (41) becomes zero and it becomes:

$$\iiint_V (\vec{E}_c^{rev} \cdot \vec{J}_c^{fwd} - \vec{H}_c^{rev} \cdot \vec{M}_c^{fwd}) dv' = \iiint_V (\vec{E}_a^{fwd} \cdot \vec{J}_a^{rev} - \vec{H}_a^{fwd} \cdot \vec{M}_a^{rev}) dv' \quad (43)$$

Where $\vec{J}_c^{fwd}$ and $\vec{M}_c^{fwd}$ denote the source reside on the Huygens's box cells, $\vec{J}_a^{rev}$ and $\vec{M}_a^{rev}$ denote the source reside on the antenna port. $\vec{E}_a^{fwd}$ and $\vec{H}_a^{fwd}$ denote the E and H field at antenna port due to IC radiation. $\vec{E}_c^{rev}$ and $\vec{H}_c^{rev}$ denote the field on Huygens's box cells due to antenna radiation.

In equation (41), J^{fwd}, M^{fwd} exist only at the source location, everywhere else J^{fwd} and M^{fwd} are equal to zero. This is also true for J^{rev}, M^{rev}. For numerical calculation convenience, the integral is implemented by using finite term summation approximation. Also the fields and current sources are further expressed in terms of voltage and current as thoroughly derived in [21]. The numerical expression of reciprocity theorem used for this study finally can be expressed as equation (44), where Z_{in} and Z_L denote the input impedance and load impedance of the victim patch antenna.

$$U_a^{fwd} = -\frac{Z_{in} Z_L}{U_a^{rev}(Z_{in} + Z_L)} \times (\sum_{cells} \vec{E}_c^{rev} \cdot \hat{n} \times \vec{H}_c^{fwd} S_{cell} + \sum_{cells} \vec{H}_c^{rev} \cdot \hat{n} \times \vec{E}_c^{fwd} S_{cell}) \qquad (44)$$

Equation (44) implies that, with tangential field obtained in forward problem and reverse problem respectively, the coupled voltage can be calculated by the tangential E and H field on Huygens's box. Hence the coupled power can be estimated.

2.2.3. Simulation Validation. Two patch antenna locating on a GND plane is used to validate the method proposed above as shown in Fig. 2.13.
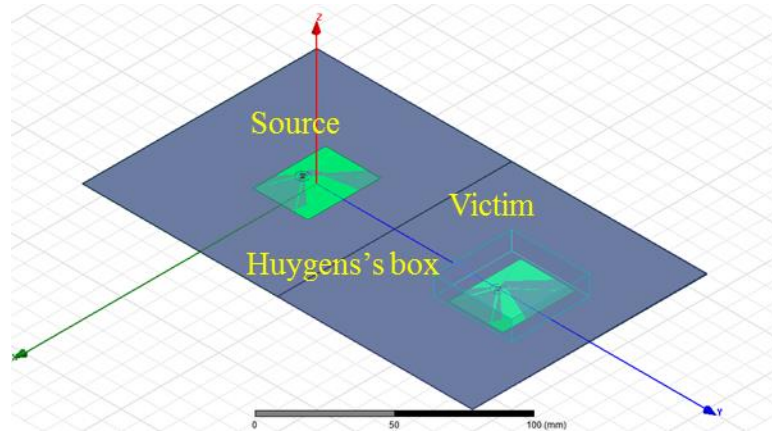

Figure 2.13. Whole simulation model of two patch antennas

The patch antenna enclosed by an imaginary Huygens's box is deemed as the victim antenna, and the patch antenna locates at the origin mimics the noise source. The patch

antenna has dimension 37.2 mm by 28 mm. And the spacing between the two patch antennas is 100 mm.

In forward problem, the victim patch antenna is removed, and the tangential E and H field on the Huygens's box due to noise source is simulated as shown in Fig. 2.14.
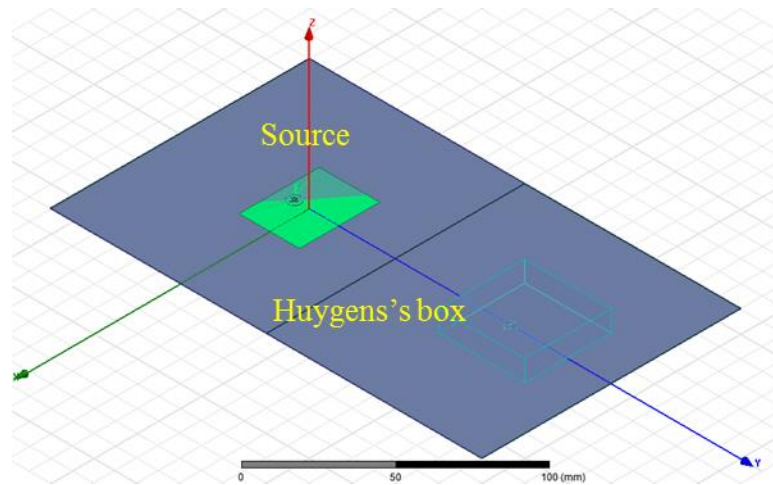
Figure 2.14. Forward problem simulation

In reverse problem, the patch antenna locates at the origin which mimics the noise source is removed, also the tangential E and H field on the Huygens's box due to victim antenna radiation is obtained as shown in Fig. 2.15.
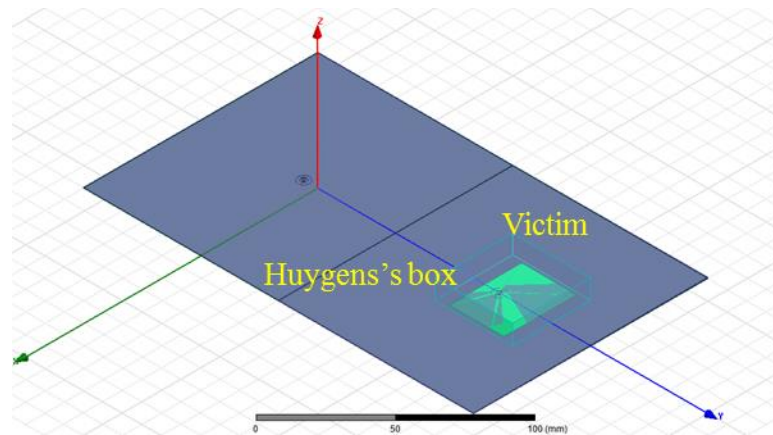

Figure 2.15. Reverse problem simulation

With the tangential field obtained in both forward and reverse problem, the transmission coefficient S21 is simulated based on simulation model in Fig. 2.13 and

calculated by the reciprocity theorem expression based on equation (44). Then the two results are compared as shown in Fig. 2.16. With S21 value and port excitation, the coupled power can be easily calculated. For simplicity, the comparison is shown by S21 value.
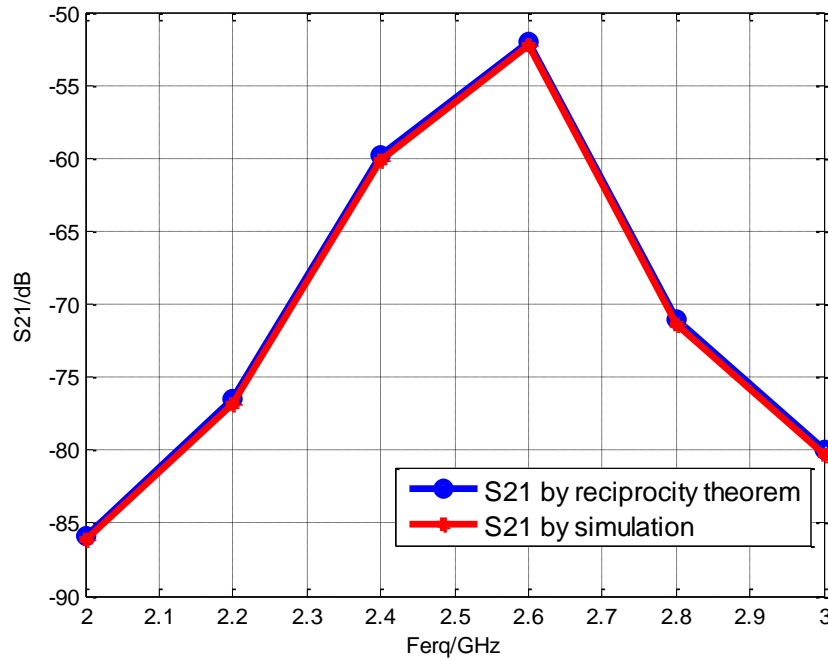

Figure 2.16. S21 comparison by direct simulation and reciprocity theorem

In this study, the noise source is modelled by Huygens's equivalent source. The noise source model in Fig. 2.13 is replaced by surface electric current with PMC boundary condition as shown in Fig. 2.17.
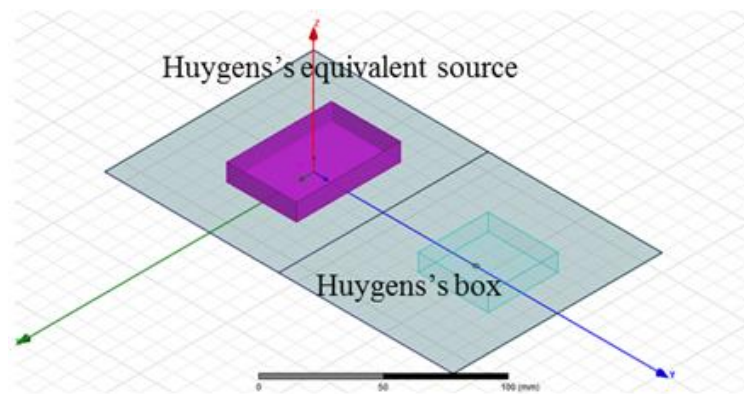

Figure 2.17. Huygens's equivalent model for forward problem

The detailed implementation of equivalent source in HFSS is described in [7]. With the source replaced by the Huygens's equivalent source, the S21 by reciprocity and by direct simulation is compared in Fig. 2.18.
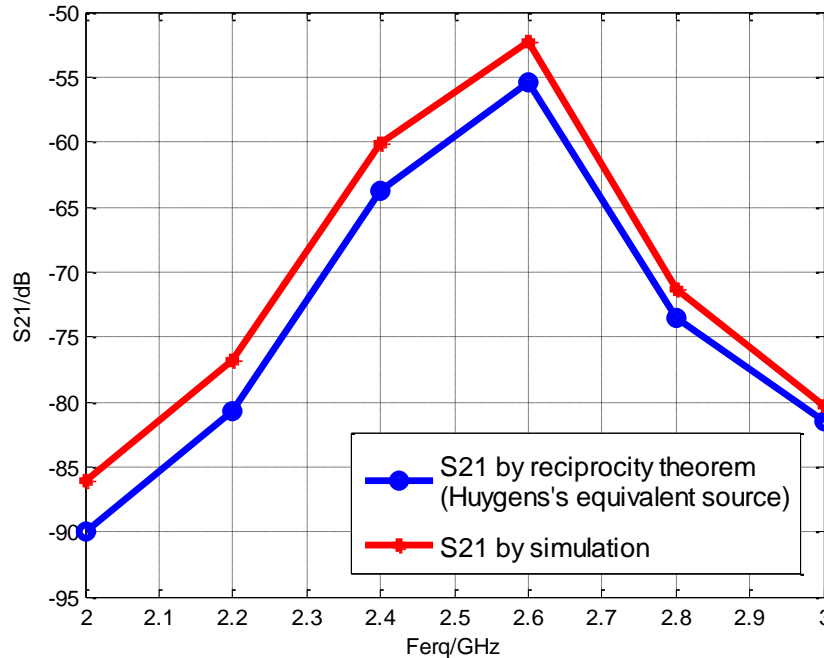
Figure 2.18. S21 comparison by direct simulation and reciprocity theorem

The difference between S21 by simulation and S21 by reciprocity theorem with Huygens's surface equivalent source is with 4 dB from 2 GHz to 3 GHz. The possible errors may come from the simulation settings like mesh size, radiation boundary size and convergence, etc.

2.2.4. Measurement Validation with Huygens's Box on Victim. A test board with a clock buffer IC and a patch antenna is measured to further validate the reciprocity method with noise source modelled by Huygens's equivalent source. The clock buffer has 8 LVPECL outputs and 2 differential inputs. The patch antenna has the same dimension as the model shown in Fig. 2.19, which is 37.2 mm by 28 mm. In the validation measurement, the patch antenna on the top left is selected as the victim antenna and the distance between the patch antenna and working IC is 50 mm. Besides, the IC board is shielded by copper tape with only IC exposed, and the GND are connected together.
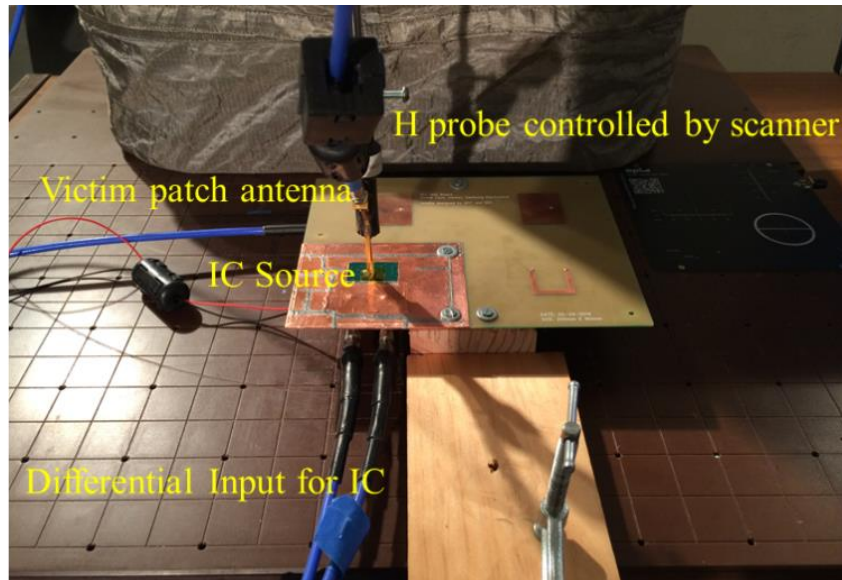
Figure 2.19. Near-field scanning for test board

In forward problem, only H field is scanned with phase information. The phase is obtained by synchronizing the probe signal with a stable reference signal which drives the IC; both of the signals are measured in oscilloscope as shown in Fig. 2.20.
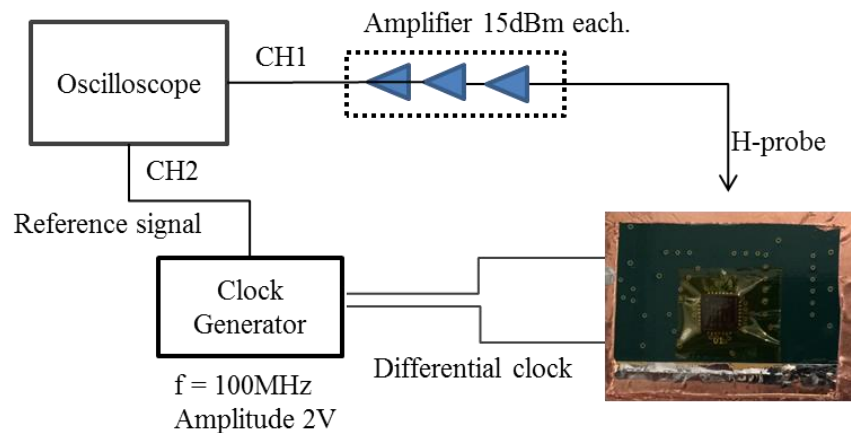
Figure 2.20. Forward problem measurement diagram

Based on the Huygens's equivalence principle, the tangential field on a closed surface is needed. In real measurement case, only tangential H field on top surface and 4 side lines are measured as shown in Fig. 2.21. The height of the side line is half of the

scanning plane which is 2.5 mm in this case. And the scanning plane size is 60 mm by 60 mm, with 1 mm spacing.
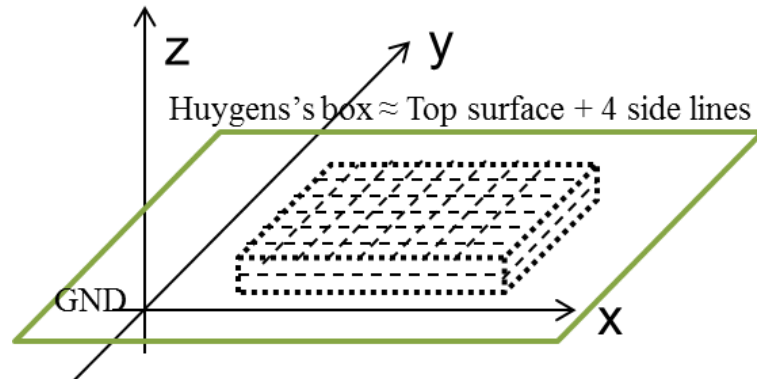
Figure 2.21. Huygens's box approximation for near-field scanning

On top surface, both tangential field Hx and Hy are measured. For x = cont. plane, only Hy is measured (Hz ≈ 0), this approximation is supported by the fact that the normal component of magnetic field on a GND plane which can be deemed as PEC is equal to 0. Although the scanning points are not right on the PEC surface, the directional derivative of magnetic field equals to 0, $\partial H/\partial n = 0$, where n is the unit normal vector pointing along z direction. Similarly, the tangential field on y = cont. plane only includes Hx component (Hz ≈ 0). Later, the field on the upper part of the side surface is set equal to the tangential field on the side line with z = 5 mm, and the field on the lower part of the side surface is set equal to the tangential field on the side line with z = 2.5 mm. The measured near-field pattern Hx and Hy of the IC selected at 2.6 GHz is shown in Fig. 2.22. The left column is magnitude and the right column is phase.

Figure 2.22. Selected Hx and Hy pattern at 2.6GHz

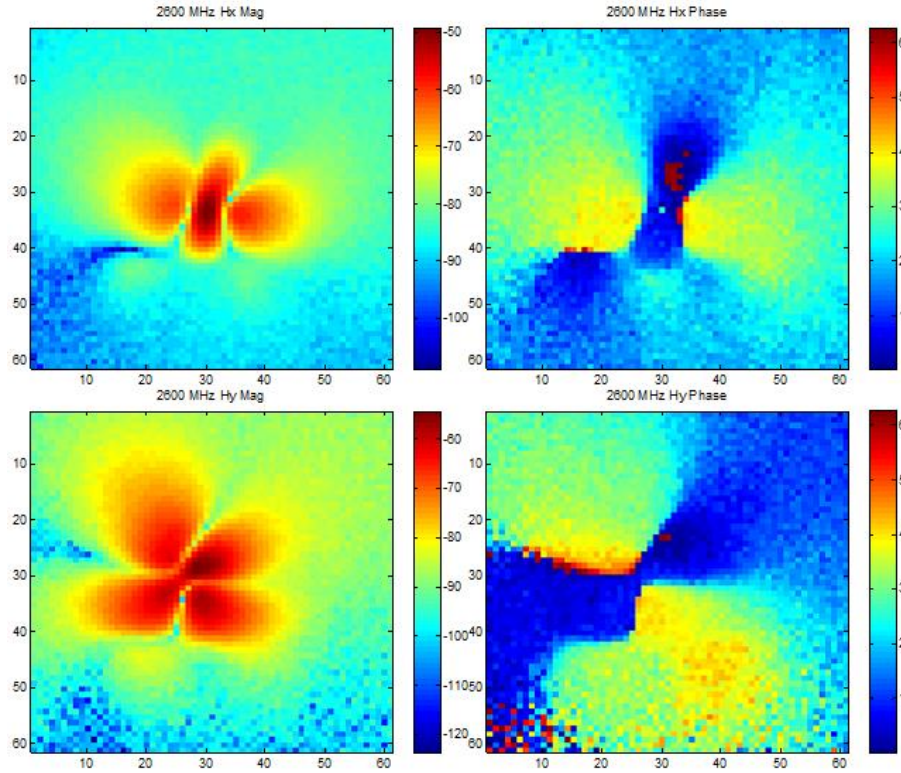With measured tangential H field on a closed Huygens's box, the equivalent near-field source can be created as described in [2][3], the corresponding simulation model is shown in Fig. 2.23.
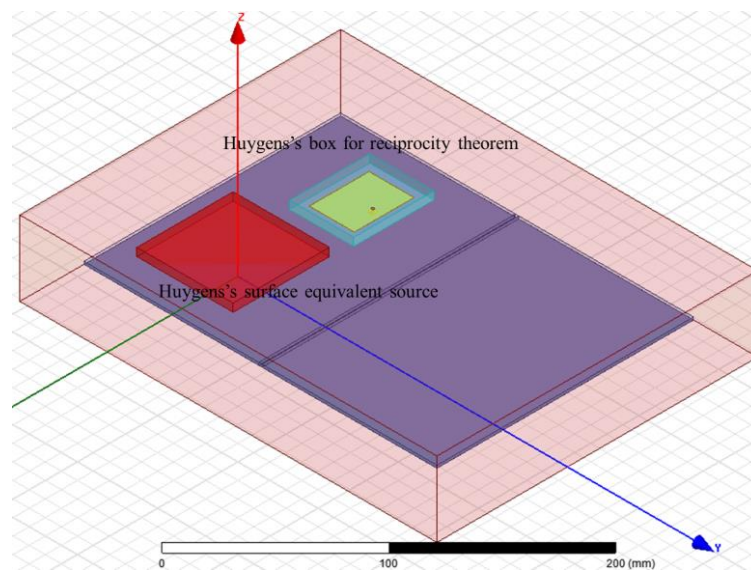

Figure 2.23. IC source replaced by Huygens's equivalent source

The tangential field on an imaginary Huygens's box is then obtained by simulation in forward problem. In reverse problem, the total excitation voltage is set to 1 V which means U_a^{rev} is equal to 1 V with matched port assumption. In addition, only the victim antenna is modelled in the simulation which is to mitigate the multiple scattering effects caused by other neighboring radiators.

With the tangential fields obtained in both forward problem and reverse problem. The coupled noise power from the working IC to victim patch antenna can be estimated by equation (44). Besides, the real coupled power is measured by a spectrum analyzer connected to the victim antenna port. The comparison between measurement and reciprocity estimation is shown in Fig. 2.24.
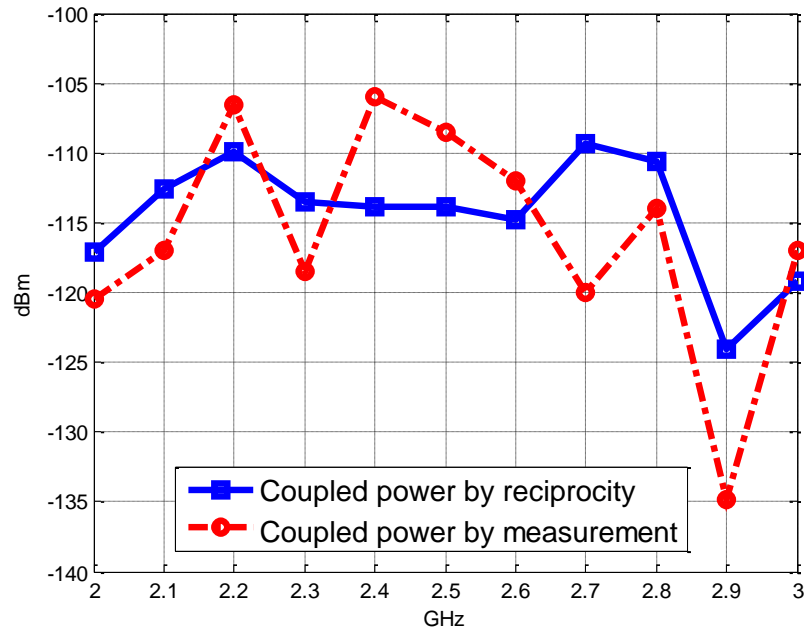
Figure 2.24. Coupled power comparison from working IC to victim antenna using Huygens's model in forward problem

The maximum difference between the power by reciprocity and measurement is within 10 dB. Errors mainly come from measurement instruments and ambient radiation. For example, measuring phase of H field by oscilloscope introduces spurious signal interference, the scanner is not well designed such that the noise generated by the motor will cause conducted emission, etc. Furthermore, there are some errors in the simulation setting like mesh size, boundary size and convergence criteria.

In forward problem, the noise source IC can also be modeled as equivalent dipole moment model based on the tangential field on the top surface. All other steps remain the same as the discussions above. The coupled power comparison using equivalent dipole model in forward problem is shown in Fig. 2.25.
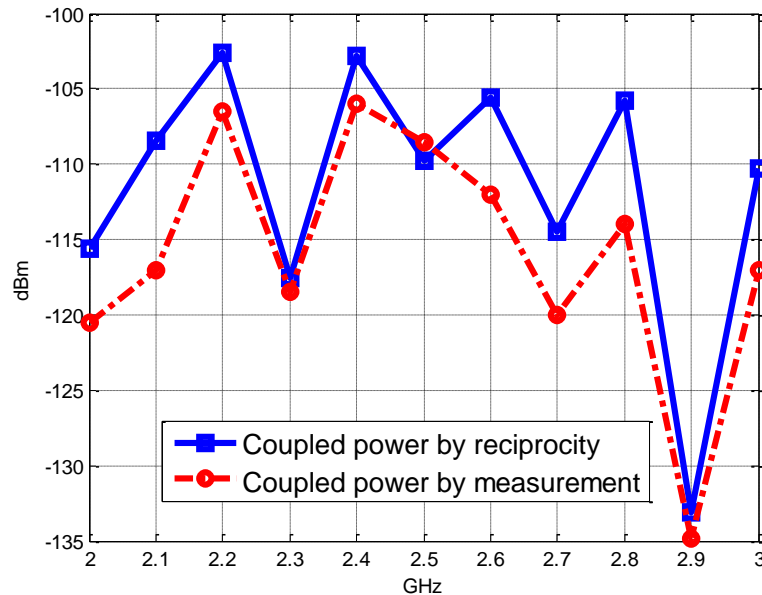
Figure 2.25. Coupled power comparison from working IC to victim antenna using dipole model in forward problem

Comparing Fig 2.24 and Fig. 2.25, the correlation between measurement and estimation by reciprocity using dipole model in forward problem is better than that using Huygens's model. There are many reasons regarding the discrepancies. On can be the multiple scattering effects and ambient radiation that changes the total field on Huygens's surface. Then the Huygens's model will be no more accurate. Another issue can be the simulation setup which is different from real measurement environment. Besides, the imperfect mesh cell size, convergence and stopping criteria will introduce extra errors.

2.3. SUMMARY AND FUTURE WORK

The whole problem is first decomposed by observing the reaction theory. In forward problem, dipole moment model or Huygens's equivalent model is extracted to equivalently represent the source IC. The tangential H field is obtained by near-field

scanning. Further, the tangential field on Huygens's box is either calculated by multiplying the dipole moments with new transfer matrix related to the Huygens's box or simulated with Huygens's model. In reverse problem, the tangential field on Huygens's box is obtained by full-wave simulation. The coupled power from IC to antenna is then estimated by reciprocity theorem. A test board with an IC and patch antenna is measured to validate the reciprocity theorem method. In [23], the author investigated the impact of scanning area on the accuracy of modeling. It is meaningful to further explore the source of errors and further improve the accuracy of entire method.

BIBLIOGRAPHY

[1]   Li, Liang, Jingnan Pan, Chulsoon Hwang, Gyuyeong Cho, Harkbyeong Park, Yaojiang Zhang, and Jun Fan. "Measurement validation for radio-frequency interference estimation by reciprocity theorem." In *Electromagnetic Compatibility (EMC), 2015 IEEE International Symposium on*, pp. 154-159. IEEE, 2015.

[2]   Li, Liang, Jingnan Pan, Chulsoon Hwang, Gyuyeong Cho, Harkbyeong Park, Yaojiang Zhang, and Jun Fan. "Near-field coupling estimation by source reconstruction and Huygens's equivalence principle." In *Electromagnetic Compatibility and Signal Integrity, 2015 IEEE Symposium on*, pp. 324-329. IEEE, 2015.

[3]   Li, Liang, Jingnan Pan, Chulsoon Hwang, Gyuyeong Cho, Harkbyeong Park, Yaojiang Zhang, and Jun Fan. " Radio-Frequency Interference Estimation by Reciprocity Theorem with Noise Source Characterized by Huygens's Equivalent Source." Accepted to be published in *Electromagnetic Compatibility and Signal Integrity, 2016 IEEE Symposium on.*

[4]   Li, Liang, Jingnan Pan, Chulsoon Hwang, Gyuyeong Cho, Harkbyeong Park, and Jun Fan. "Application of Reciprocity Theorem in Radio Frequency Interference Estimation." Accepted to be published in *Electromagnetic Compatibility and Signal Integrity, 2016 Asia-Pacific International Symposium on.*

[5]   Wilson, P. "On correlating TEM cell and OATS emission measurements."*Electromagnetic Compatibility, IEEE Transactions on* 37, no. 1 (1995): 1-16.

[6]   Yu, Zhenwei, Jason A. Mix, Soji Sajuyigbe, Kevin P. Slattery, and Jun Fan. "An improved dipole-moment model based on near-field scanning for characterizing near-field coupling and far-field radiation from an IC."*Electromagnetic Compatibility, IEEE Transactions on* 55, no. 1 (2013): 97-108.

[7]   ANSYS HFSS 2014 from ANSYS Inc. [Online]. Available: http://www.ansys.com/ May 7, 2016.

[8]   Yu, Zhenwei, Jayong Koo, Jason A. Mix, Kevin Slattery, and Jun Fan. "Extracting physical IC models using near-field scanning." In *Electromagnetic Compatibility (EMC), 2010 IEEE International Symposium on*, pp. 317-320. IEEE, 2010.

[9]   Balanis, Constantine A. *Antenna theory: analysis and design*. John Wiley & Sons, 2016.

[10]   Strang, Gilbert. *Introduction to linear algebra*. Vol. 3. Wellesley, MA: Wellesley-Cambridge Press, 1993.

[11]   Zhang, Ji, Keong W. Kam, Jin Min, Victor V. Khilkevich, David Pommerenke, and Jun Fan. "An effective method of probe calibration in phase-resolved near-field scanning for EMI application." *Instrumentation and Measurement, IEEE Transactions on* 62, no. 3 (2013): 648-658.

[12]   T. Li, V. Khilkevich and D. Pommerenke, "Phase-Resolved Near-Field Scan Over Random Fields," in *IEEE Transactions on Electromagnetic Compatibility*, vol. 58, no. 2, pp. 506-511, April 2016.

[13]   Matlab R2014a from MathWorks Inc. [Online]. Available: http://www.mathworks.com/ May 7, 2016.

[14]   Tong, Xin, D. W. P. Thomas, A. Nothofer, P. Sewell, and C. Christopoulos. "A genetic algorithm based method for modeling equivalent emission sources of printed circuits from near-field measurements." In 2010 Asia-Pacific International Symposium on Electromagnetic Compatibility. 2010.

[15]   Tong, Xin. "Simplified equivalent modelling of electromagnetic emissions from printed circuit boards." PhD diss., University of Nottingham, 2010.

[16]   CST – Computer Simulation Technology. [Online]. Available: https://www.cst.com/ May 7, 2016.

[17]   J. Pan, L. Li, X. Gao and J. Fan, "Application of dipole-moment model in EMI estimation. " *2015 IEEE International Symposium on Electromagnetic Compatibility and EMC Europe*, Dresden, 2015, pp. 350-354.

[18]   J. Pan, X. Gao and J. Fan, "Far-field prediction by only magnetic near fields on a simplified Huygens's surface." *IEEE Trans. Electromagn. Compat.,* vol. 57, no. 4, pp. 693-701, Aug. 2015.

[19]   J. Pan, H. Wang, X. Gao, C. Hwang, E. Song, H. Park and J. Fan, "Radio-frequency interference estimation using equivalent dipole-moment models and decomposition method based on reciprocity. " *IEEE Trans. Electromagn. Compat.,* vol. 58, no. 1, pp. 75-84, Feb. 2016.

[20]   J. Pan, X. Gao, Y. Zhang, J. Fan, "Far-field radiation estimation from near-field measurements and image theory." in *Proc. IEEE International Symposium on Electromagnetic Compatibility.,* Raleigh, NC, Aug. 2014, pp. 609-614.

[21]   Wang, Hanfeng, Victor Khilkevich, Yao-Jiang Zhang, and Jun Fan. "Estimating radio-frequency interference to an antenna due to near-field coupling using decomposition method based on reciprocity." *Electromagnetic Compatibility, IEEE Transactions on* 55, no. 6 (2013): 1125-1131.

[22]   Balanis, Constantine A. *Advanced engineering electromagnetics*. Vol. 20. New York: Wiley, 1989.

[23]   Ren, Xiao, Pushp Maheshwari, Yao-Jiang Zhang, Victor Khilkevich, Jun Fan, Yan Zhou, Yadong Bai, and Xuequan Yu. "The impact of near-field scanning size on the accuracy of far-field estimation." In *Electromagnetic Compatibility (EMC), 2014 IEEE International Symposium on*, pp. 582-587. IEEE, 2014.

VITA

Liang Li was born in Yichun, Jiangxi Province, China. He received his B.S. degree in Electronics and Information Engineering from Huazhong University of Science and Technology, Wuhan, China, in 2013. He joined the EMC Laboratory in the Missouri University of Science and Technology, Rolla, in 2013 and received the M.S. degree of Electronic Engineering in July 2016. He worked as a Signal Integrity Engineer Intern at Cisco in 2015. He received Best Student Paper Award from IEEE Electromagnetic Compatibility Society in 2015.